UNIVERSITY OF CALIFORNIA
SANTA CRUZ

DEEP AND FAST HIGH-RESOLUTION 3D MICROSCOPY

A dissertation submitted in partial satisfaction of the
requirements for the degree of

DOCTOR OF PHILOSOPHY

in

ELECTRICAL AND COMPUTER ENGINEERING

by

Eduardo Hirata Miyasaki

September 2022

The Dissertation of Eduardo Hirata Miyasaki
is approved:

Assistant Professor Sara Abrahamsson, Chair

Associate Professor Mircea Teodorescu

Associate Professor Shiva Abbaszadeh

Senior Scientist Jennifer Morgan

Peter Biehl
Vice Provost and Dean of Graduate Studies

Table of Contents

List of Figures

List of Tables

Abstract

Deep and Fast High-Resolution 3D Microscopy

by

Eduardo Hirata Miyasaki

Acquisition speed in high-resolution imaging in three dimensions (3D) remains a major challenge in modern microscopy. When 3D information is collected sequentially, acquisition speed is limited and increases with the sample volume size imaged. Aberration-corrected multifocus microscopy (MFM) employs diffractive Fourier optics to multiplex and refocus the microscope image to enable truly simultaneous 3D imaging, without loss of resolution. This thesis describes a new type of ultra-fast 25-camera-array multifocus microscope (M25) which employs an array of small, fast CMOS cameras sensitive enough for live 3D fluorescence imaging. The use of multiple sensors allows M25 to significantly push acquisition speed, depth or field, and field of view to capture $130\times130\times50$ μm^3 volumes at ~100 Hz. This new optical design also employs a radically simplified chromatic correction module from classical MFM systems, consisting of simple pairs of diffractive elements. The prototype instrument here described is customized for functional neural circuit imaging and locomotion in small model organisms and is demonstrated on *Caenorhabditis elegans*, fruit fly (*Drosophila melanogaster*), and lamprey (*Petromyzon marinus*).

To my family, Yasu, Mimi,Hiro

Acknowledgments

I cannot thank enough my advisor, Sara Abrahamsson, for teaching me the beauty of live-3D imaging, her mentoring, and discussions. I am truly grateful to be the first Ph.D. student graduating from her lab. Thank you to all SaraLab members, to Antone Bajor, Gustav Petterson, Maximilian Senftleben, Marc Reinig and Maximus who have made building and imaging in the dark room a fun laser party. Thank you to all my friends that I made through the years in Santa Cruz making it a fun place and sharing quality time surfing, hiking, rock climbing, beach bonfires,and game nights. Special thank you to Jennifer Morgan, Kaitlyn Fouke, Cristina Roman-Vendrell, Karina Vargas Barria, and all the amazing Morgan Lab members for hosting me and letting me work with the lampreys. This work would not have been done with the fantastic people and support from the Marine Biological Laboratory: Louie Kerr, Jim Mcillvain, Dana Mock-Munoz, the 2019 Neurobiology course and the 2019 AQLM Course. Thank you to our collaborator Gal Haspel for the *C.elegans* samples, guidance, and opportunity to handle these nematodes. Thank you Thomas Graham for the first live *Drosophila* samples for the M25. Thank you to my UCSC committee members Professors Mircea Teodorescu and Shiva Abbaszadeh for guidance and helpful feedback.

Finally I want to thank my family, my late grandparents Jesus Hirata Tahara and Kyoko Okamoto Oda, and Isabelle Chevallier for unconditional

love and constant support.

Chapter 1

Introduction

This dissertation describes the design, development and implementation of an ultra-fast, truly simultaneous, high-resolution 3D microscopy system, employing diffractive Fourier optics for multi-focus microscopy capability. Biological research today and through history relies heavily on microscopy to visualize and investigate the structures and processes of life both *in vitro* in human tissue and cell culture and and *in vivo* in model organisms such as yeast cells, fruit flies, nematodes and fish. Innovations in the field of optics are actively driving biological research and live 3D imaging at high speed and high resolution has the potential to open up new fields of research in biology and biomedicine. The instrument here described, an ultrafast Multifocus 25-camera-array microscope (M25), focuses on applications in functional neuronal imaging with fluorescence microscopy. Indicators of neural activity such

as calcium indicators enable the direct visualization of neuronal signaling in living organisms where 3D acquisition speed and resolution are essential.

I first present our approach to tackle the classical problem of high-speed 3D imaging, which remains a major challenge in modern microscopy and in particular when visualizing fast and dynamic biological processes that occur in the millisecond regime, such as molecular signaling or neural activity, particularly in locomotion of freely-moving organisms. In essence, temporal and spatial resolution are fundamentally working against each other in classical 3D image formation. In live 3D biological imaging, the main trade-offs are: speed, size of imaging volume, and sensitivity.

Aberration-corrected multifocus microscopy (MFM)[1] provides a powerful solution to the 3D high-speed imaging problem. In MFM, the image beam from an optical microscope is multiplexed and refocused by a single diffractive element to simultaneously project multiple focal planes into one image plane. The focus stack is thus laid out in an array of focal planes, allowing simultaneous capture of an entire specimen volume. MFM does not reduce image resolution since the multifocus diffractive element—the multifocus grating (MFG)—is placed in the Fourier plane of the image path and removes the spherical aberration that would otherwise be introduced when the objective is used away from the nominal focal plane. MFM thus allows for truly simultaneous, fast, high-resolution 3D imaging of biological specimens and is

compatible with super-resolution microscopy [2] and localization microscopy [3]. MFM images have classically been implemented in an optical design which images the focus stack array onto a single image sensor. This approach limited the image volume due to the limited number of pixels on the single sensor.

This dissertation describes the development of a new optical design for multifocus microscopy. It employs an array of small, fast, and sensitive CMOS cameras laid out in a 5x5 array which simultaneously and separately capture 25 focal planes to render deep 3D volumes. Importantly, the new optical design includes a radically simplified chromatic dispersion correction approach compared to previous multifocus microscopes. Optimized for functional neural circuit imaging, the M25 prototype captures $130\times130\times50\mu m^3$ volumes, with focus step between consecutive focal planes of $2\mu m$ at >100Hz. The M25 instrument is now employed to study neural circuit function in various small model organisms.

Chapter 2 describes capabilities and challenges in wide-field and fluorescence microscopy, 3D imaging techniques, spatio-temporal trade-offs, and the aberration-free multifocus microscopy method.

In chapter 3, we describe the optical principles and the development of the Multifocus 25-camera-array microscope. The original MFM design [1] employed a chromatic dispersion correction strategy based on a combination of diffractive and refractive elements, which has here been radically simplified

to a pair of diffractive elements which completely remove dispersion across the entire spectrum of light. Thus all custom parts of M25 can be manufactured hands on. We have manufactured ours hands-on in the open-academic nanofabrication facility at UCSB.

In chapter 4, we showcase the applications and uses of the M25 in live 3D biological imaging of neural circuit function in lamprey (*Petromyzon marinus*) and zebrafish (*Danio rerio*). We characterize the instrument Point Spread Function and show speed of imaging with 100 Hz fluorescent beads diffusion in water and live imaging of beating heart in the *Drosophila* embryo. Additionally, we show a pilot study of neural signaling in locomotion in the *C.elegans* embryo. These experiments demonstrate the M25 system's speed and sensitivity in large 3D volumes.

Chapter 5 describes our work on hardware control electronics to allow simultaneous acquisition from 25 cameras each running at $\sim$ 100 Hz and the data handling challenges involved. We also describe our user friendly data acquisition solution. This is implemented using open source software.

Chapter 6 is an outlook of the future applications and developments of M25 imaging in biology.

In the appendices, we provide resources for home builders of optical microscope in form of drawings, diffractive optics design software, and protocols for optical nanofabrication.

Chapter 2

Background

2.1 Optical Microscopy

2.1.1 Wide-Field Microscopy

The classical optical microscope is known as the wide-field microscope and forms a 2D image that is similar to the image formed in a photographic camera, but with higher resolution and very short depth of focus. Microscope optics have been perfected over hundreds of years and their objective lenses are today virtually aberration-free. Their objective lenses typically have extremely large numerical apertures (that is, they collect light over a large solid angle) and render exquisite resolution both laterally and axially. Modern wide-field microscopes employ an 'infinity corrected' objective lens in combination with a tube lens. The objective and tube lens are placed at a distance from each

other that is equal to the sum of their focal lengths and the microscope objective thus outputs a collimated beam of light from each point on its front focal plane. This beam is in turn focused by the tube lens to form a planar 2D image at the back focal plane of the tube lens, which is the microscope primary image plane. (Fig 2.1). High magnification is obtained since the focal length of the objective is very short while the focal length of the tube lens is long. The back focal plane of the objective is known as the the pupil stop or aperture stop is the Fourier plane of the imaging system [4].

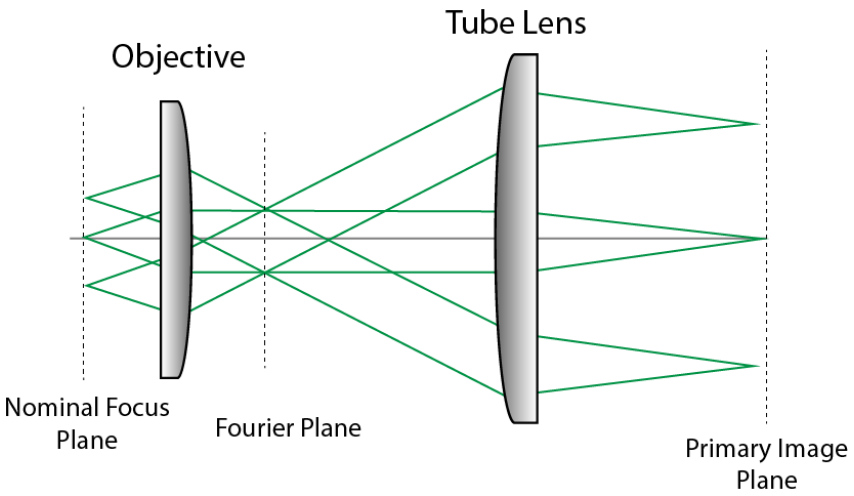

Figure 2.1: Wide-field Optical Microscope. Infinity corrected objective lens in combination with Tube Lens to form a well corrected image from nominal focus plane to primary image plane

Biological tissues and organisms which are semi-transparent are particularly well suited for optical microscopy. Reflected or transmitted light from a lamp or other source can be used to illuminate the specimen. The image is formed by diffraction [5]. Different modalities to obtain contrast in unlabeled

specimens imaged with transmitted light include Direct Interference Contrast, Phase contrast and polarization.

2.1.2 Fluorescence Microscopy

In fluorescence microscopy, the light that forms the image is not formed from illumination light transmitted through the sample, but instead emanates from fluorescent molecules with which the sample has been labeled. Fluorescence is the light phenomena that occur when the fluorescent molecule is excited by energy from an incoming absorbed photon. (Excitation can occur in form of a change of the molecule's rotational, vibrational, and electronic states.) After having been excited, the fluorescent molecule then de-excites, emitting a photon. This is a rapid process of photon excitation (~ femtoseconds) followed by de-excitation and photon emission (~ nanoseconds).

The excitation energy spectra across which a certain fluorophore is able to, respectively, absorb and emit light is described by the Jablonsky diagram (Fig2.2(a)). The difference in energy is called the Stokes shift (Fig2.2(b)). The relation between photon energy E and wavelength λ is E=hc/λ where h is Planck's constant and c is the speed of light. Typically, the emitted photon has lower energy than the incoming exciting photon meaning the fluorescence emission light is of a different color (longer wavelength) than the excitation light. For example, the commonly used fluorophore called Green Fluorescent

Protein is excited by blue light and emits green light [6].

Fluorescent probes come in variety of absorption and emission spectra. [7]. Tiny organic dye molecules can be conjugated to antibodies that stick to specific proteins inside cells that are to be visualized. A major recent advancement in biological microscopy in the last decades has been the development of genetically expressed fluorescent proteins or marine origin to tag individual proteins in living organisms. By labeling different proteins with multiple colors, fluorescent labeling makes it possible to visualize the internal structures of cells and their dynamic interactions with each other with incredible specificity Fig2.2 (a).

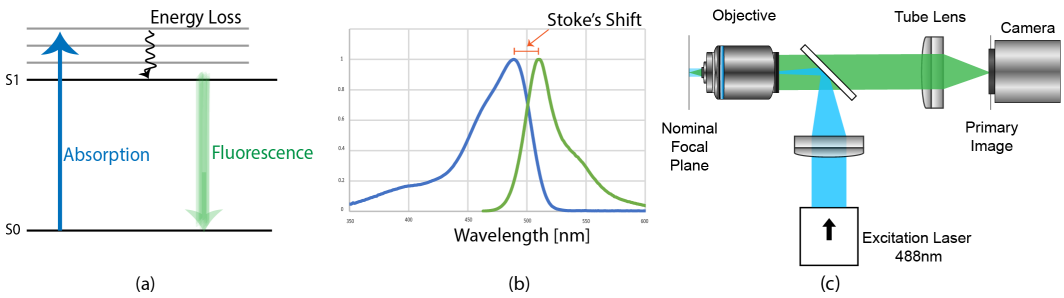

Figure 2.2: Fluorescence Microscopy (a) Jablonsky Diagram of fluorophore absorption and emission of photons. (b) Stoke shift example on GFP excitation and emission spectra. (c) Fluorescence microscopes are typically configured in epi-illumination, where the excitation and emission beams pass through the same objective. In order to separate the emission from excitation light, a dichroic mirror is placed in the beam path at 45° angle.

The most common method for fluorescence microscopy setups is the epi-illumination method in which the configuration uses single objective for exci-

tation and emission and it is composed mainly of 4 components: the objective, the tube lens, dichroic filter and the imaging sensor Fig2.2(c). In, most configurations, fluorescence microscopy can be done by placing a dichroic filter, which allows one to split the excitation from the emission spectra going into or away from the sample. Additionally, emission or excitation filters can be placed in the path to clean up the signal based on the experiment, tissue, and fluorophores of interest due to autofluorescence, narrow excitation bands or fluorescence cross-talk. Fluorescence microscopy detection relies on bright, stable, and low-phototoxic probes so the signal emitted by the fluorophores can be detected.[8]

2.1.3 Confocal and light-sheet microscopy

Confocal microscopy is widely used in biological microscopy, with the advantage of optical sectioning (rejection of out-of-focus fluorescence light) which provides high signal contrast also in a densely labeled specimen. Confocal microscopy however relies on scanning through the sample both laterally—to collect each 2D image plane—and axially—to collect the stack of 2D planes that that constitutes the microscope 3D image. In recent years, light-sheet microscopy systems of various modalities have become popular for collecting 3D volumes with highly optical-sectioned images by sequentially and coordinately swiping a sheet of light across the sample to acquire a 3D rendering of the sam-

ple through a 2D focal stack[9][10][11][12][13]. Light-sheet microscopes have the additional advantage over confocal microscopes of increasing sensitivity by limiting the light dose received by the living sample. However, the sequential nature of image acquisition of both confocal and light-sheet microscopy can be time-consuming even with high-speed hardware, and acquisition speed decreases with the size of the volume imaged. Thus, 3D acquisition time can in practice be limiting in living samples. Classical wide-field fluorescence microscopy is therefore, despite its lack of optical sectioning, sometimes the only realistic alternative when imaging very fast events such as neuronal signaling [14], [15], [16].

In classical wide-field microscopy, each 2D plane is formed and recorded simultaneously, just like in a photographic image. Scanning is done through focus in order to sequentially collect the set of focal planes that constitutes the 3D image (focus stack)[17]. Even here, the sequential scanning through focus takes precious time, even when using high-speed piezo-electric stages. Spatial and temporal resolution are working against each other in all scanning imaging modalities.

2.1.4 Resolution of the optical microscope

No matter how much we magnify an image, there is a limit to how fine details in the sample we can resolve. This limit is known as the diffraction

limit of resolution and is set by the numerical aperture (NA) of the imaging system and the wavelength λ of the light which we image. Light captured from the specimen can be described by the superposition of spherical waves propagating across all spatial directions. The content of an image can thus be modeled as a Fourier series of spatial frequencies in the sample. Since higher spatial frequencies (finer details) diffract light stronger, optical imaging systems are band limiting devices due to the limited acceptance angle of their aperture. Very fine spatial frequencies diffract light too strongly to be gathered by the aperture and cannot be resolved. The Numerical Aperture is specified as $\mathrm{NA} = \mathrm{n} \cdot \sin\alpha$ where n is the refractive index of the immersion medium and α is the half angle over which the objective collects light. Thus the objective acts as as a band-pass filter for higher spatial frequencies. Features smaller than the resolution limit of the imaging system can be detected, but not resolved. An infinitely small point-source of light in the specimen is imaged as a blurry spot. The shape of the blur spot resulting from a point source in an imaging system is called the Point Spread Function. In a microscope with an objective that is free from optical aberrations, this blur spot has the shape of the Airy disk pattern. According to the Abbe criterion, the resolution attainable by the wide-field microscope is defined for lateral resolution according to eq2.1 and axial resolution according to eq 2.2. [4]

$$LateralResolution = d_{xy} = \frac{\lambda}{2 \cdot NA} \tag{2.1}$$

$$AxialResolution = d_z = \frac{2 \cdot \lambda}{NA^2} \tag{2.2}$$

In practice, the classical wide-field light microscope can obtain up to ≈200nm lateral resolution and ≈500nm axial resolution.

2.2 The 3D image

2.2.1 The Focus Stack

As discussed, the wide-field microscope forms a 2D image of a single focal plane of the specimen. Due to the large aperture (high NA) of the microscope objective, the microscope image has a very short depth of focus. This enables the observer to discern between different focal planes of the specimen as the focus is scanned in the axial (z) direction. By recording a focal stack of thinly sliced 2D images and combining these computationally we can form a 3D image of the specimen Fig 2.3.

Using fast piezo-electric z-stages with exquisite precision for mechanical refocusing and synchronizing the stage with the camera exposures, the focal stack of images can be formed very quickly. From the thin 2D image slices of

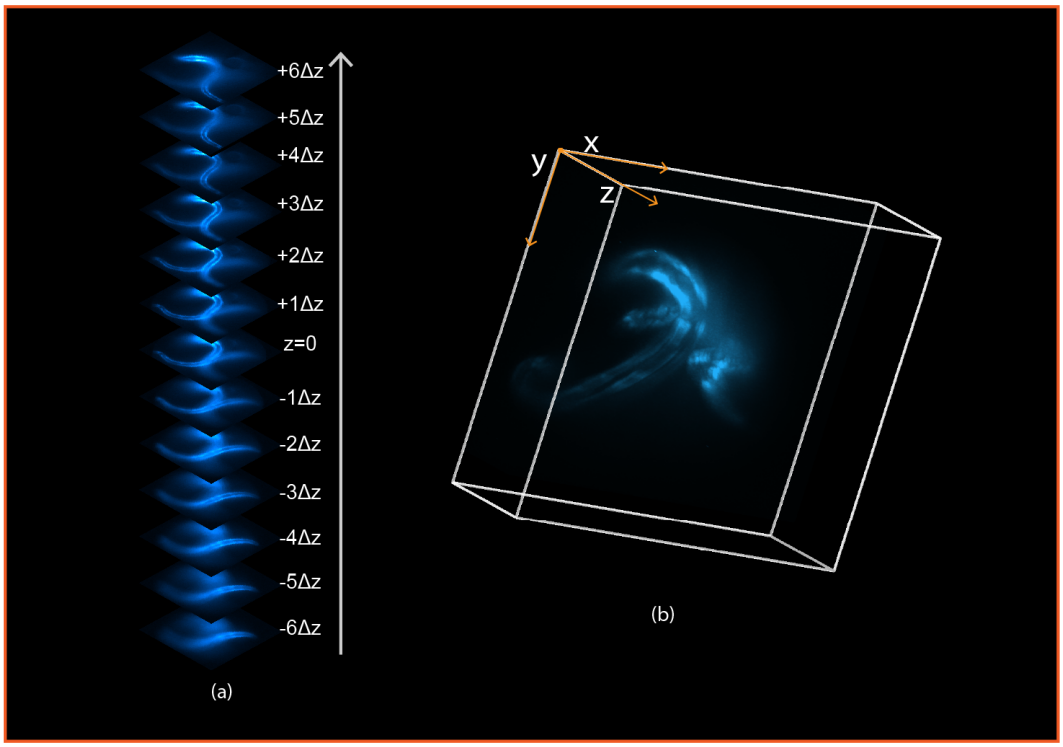

Figure 2.3: A 3D image consist of a series of 2D images with equally spaced focus shift (a) Representation of a focal stack of 2D images to render a 3D image. Traditional microscopy systems mechanically scan through focus and collect 2D slices to render combine computationally and render a 3D image (b) Combination of focal stack computationally to visualize and analyze volumetric information

the focal stack, the 3D image is then generated computationally. Still, when imaging the fastest dynamic biological processes, this method for collecting a focal series can be too slow. Ultimately the limit to acquisition speed is the acquisition time per frame of the camera—which is limited by both the shortest read-out time of the camera sensor (~milliseconds) and the exposure time required to obtain enough signal to form an image—multiplied with the number of focal slices of the 3D stack, plus the time of refocusing (~milliseconds).

It can be noted that an additional problem with mechanical refocusing is

that the movement of the stage during focus scanning can disturb the specimen. An elegant solution to the mechanical refocusing problem is remote-refocusing methods, where a telescope lens setup is constructed to perfectly re-image the image plane using two objectives whose magnification ratio equal the refractive index. Remote refocusing can also be achieved with electronic tube lens at very high speed, for example 17 planes at 510frames per second equivalent to 30 volume scans per second [18]. Remote focusing however still relies on the somewhat time-consuming process of recording 3D information sequentially and on multiple image exposures. [19].

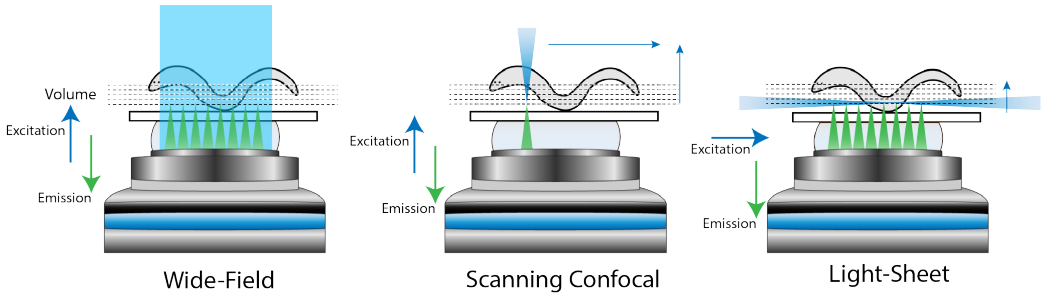

Figure 2.4: Common fluorescence microscopy 3D imaging techniques: Wide-field, scanning confocal and light sheet microscopy.

2.2.2 Methodologies for Single Shot 3D Imaging

Methodologies for imaging a 3D volume can be categorized as either simultaneous (single shot) or parallel (sequential) data acquisition using either multiple sensors or sequential acquisition. Single shot 3D imaging is an active field of research in optics and different approaches are being developed.

A conceptually interesting imaging method for simultaneous capture of 3D information is light-field microscopy (LFM) [20] , which uses a microlens array placed in the beam path in a configuration similar to that of a Shack-Hartman wavefront sensor. LFM is capable of collecting 2D information of the location and the angle of the incident light, for which one can reconstruct a 3D volume. [21] [22]

These methods in their current implementations however inherently suffer from spatial (lateral and axial) loss of resolution and uneven spatial resolution across the sample. Image reconstruction is intricate and especially in fluorescence microscopy prone to reconstruction artefacts from stray light or out-of-focus light emission. The method is however conceptually interesting and may have applications in photography depth ranging [23].

For reliable and unambiguous simultaneous "single shot" 3D imaging without temporal ambiguity, the simultaneous recording of multiple 2D focal planes remains highly attractive. An early approach for obtaining multiple simultaneous focal planes was placing one or two beam-splitters in the imaging path of a microscope and roughly refocusing these to image two or three focal planes simultaneously [17]. In the simplest case, one of the cameras can be moved away from the nominal focal plane to obtain a rough refocus. This method can be used to capture a few image planes into a camera sensor at offsets[24] or onto individual cameras [25]. Diffractive Fourier optics can also be used to

multiplex and refocus the light [26]. Early implementations of simultaneous imaging of multiple focal planes have comes at the cost of loss of resolution through optical aberration. Objective lenses are designed for aberration-free imaging only at the nominal focus. When the objective lens is used to image a specimen plane that is away from the nominal focal plane, depth induced spherical aberration will begin to deteriorate the image after a few micrometers of defocus. This effect is especially strong in high-NA objectives. To avoid deterioration of resolution, an aberration-free refocusing method must be used. Aberration-corrected Multifocus microscopy (MFM) [1] is a simultaneously captured 3D microscopy method that does not compromise resolution by either loss of information or introduction of aberrations and is the basis of the imaging system described in this dissertation, and is described in detail in the following chapters.

2.3 Imaging Neuronal Function

The use of fluorescence microscopy has revolutionized the field of biology as it enables the study of targeted biomolecules and proteins in living organisms by directly measuring the chemical or electrical signals inside the living specimen. Although these measurements can be collected through other methods with higher temporal resolution such as eletrophysiology, optical approaches have been preferred as they are minimally invasive and allow for simultaneous

imaging of multiple neurons at a single cell-resolution. To achieve this, the development of fluorescent probes has focused on calcium ions as this versatile chemical plays big roles in many biological processes including: inter-cellular signaling, gene transcription regulator, and cytoskeletal dynamics. Specifically in neurobiology, calcium plays an important role as intercellular messenger in neurons and be utilized to measure the calcium transients in individual presynaptic terminals, dendritic integration, voltage propagation and dendritic spiking [27]. For example, at rest calcium concentrations are about 50-100nM and rise during electrical activity of from 10 to 100 times higher [28]. These rapid changes in the flux of calcium can be paired with calcium image probes to detect and visualize activity in living neurons. In cortical neurons, the intercellular calcium rise 150nm is within 10ms which then falls at a half decay time of 50-70ms [29]. This means fast and sensitive optical imaging techniques must be developed in combination to bright, sensitive, and photo-stable calcium indicators.

The two most common methods for calcium imaging are the genetically encoded calcium indicators(GECIs) and the dye-loading methods. The GECIs can be engineered from various proteins to respond to neuronal events. These optical reports can be transinfected using viral vectors and used to study an organisms while swimming, eating, moving, or developing. For most studies performed in this thesis, we primarily used the GECI from the GCaMP family

due to it's brightness, speed, and stability to measure activity in freely moving organisms These GCaMP are a compound of enhanced green fluorescent protein (EFGP) paired with cadmodulin, a calcium binding proteins to measure rise and decay kinetics [30]. Additionally, the alternate methods to GECIs is the dye-load calcium indicators into neurons through acute network loading, dextran-conjugate loading or bulk electroporation [27]. For this methods, the dye is micro injected to the spinal cord neurons to allow the cells take the dye for imaging. This technique is useful to identify synaptically connected neurons, analysis for the circuitry and population of neurons and study neuron populations intracellular calcium influx and release [31].

Since action potentials (AP) are initiated around 3-5 ms before the calcium transient reaches the peak, the slow kinetics must be captured at an order of magnitude longer than the APs itself. This limits the ability to use the GECIs or dyes for detecting fast and multiple AP that are masked under one calcium transient. GECIs recorded singals are heavily influence by the response characteristics, so sufficient responsiveness and speed to report neural events. Along the calcium imaging probes, the development and advances of these depend on the development of the imaging techniques to study these transients.

The need for faster, brighter and stable calcium indicators is strikingly apparent when looking at axonal spikes can occur singly or in bursts at fre-

quencies >100Hz. To measure this activity, there has been a push to measure the transmembrane voltage using genetically encoded voltage indicators measuring activity in the millisecond regime. Probes like ArcLight which has been used to detect APs and subthreshold depolarization events in single cells has been utilized but is still limited by activation and deactivation slow kinetics of 10ms and 28ms respectively [15].

Advances in microscopy techniques have allowed sensitive and high-contrast imaging with light-sheet microscopy [32], confocal microscopy [7], and spinning disk confocal[33], and deeper and high-resolution with two-photon [34]. However, all of these methods perform sequential scanning for acquiring 3D information as discussed above, so high-resolution, fast and sensitive methods are needed in development.[29]

2.4 Aberration-corrected Multi-focus Microscopy (MFM)

While simultaneous 3D imaging is of the essence in biological imaging, most simultaneous / single shot 3D imaging systems suffer from aberrations which limit resolution and sensitivity. Aberration-corrected multifocus microscopy employs diffractive Fourier optics to obtain aberration-free refocusing.

2.4.1 Aberration-free Refocusing

In order to achieve aberration-free 3D imaging Abbe's sine condition and Hershel's condition must be satisfied. In this manner, it is possible to perfectly form a focused image both laterally and axially. Abbe's sine condition states the spatial frequencies from the object to images space must scale eq2.3.

$$\begin{aligned} \rho &= sin(\theta)/sin(\alpha) \\ sin^2(\theta) &= \rho^2 \times sin^2(\alpha) \end{aligned} \tag{2.3}$$

In commercial microscope systems, this condition is satisfied by making well corrected objective and tube lens pairs for are a single planar plane. This means that as one starts to image outside of the nominal focal plane for which the objective is designed, the introduction of spherical aberrations is prominent, destroying the resolution of the system Fig 2.3. If the wavefronts are distorted or the spatial frequencies are not scaled properly, the reconstruction from object to image will not produce high-resolution images. For these well-corrected optical systems, a ray angle θ in the sample plane corresponds to a position in the back focal plane of the objective, also called the pupil plane, which is the Fourier plane of the imaging system. This allows one to calculate the out-of-focus phase error from a point source on the optical axis in a focal plane at defocus δz and counter it by introducing geometrical distortion in the

pupil plane to compensate for the phase-error for each point in the pupil plane Fig2.3(b).

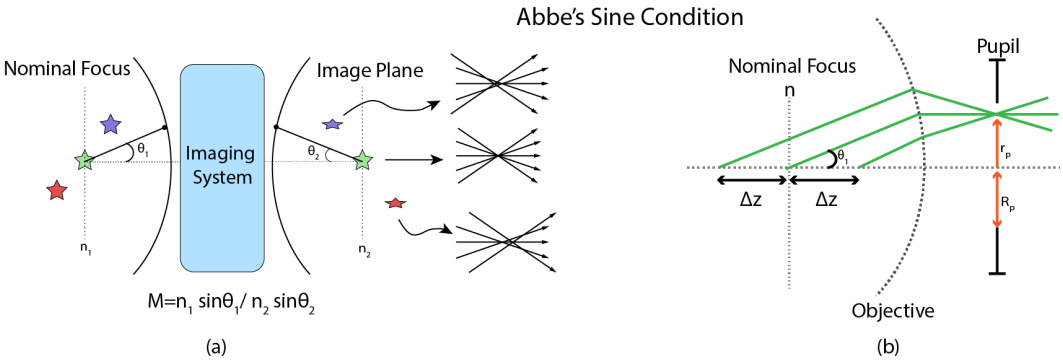

Figure 2.5: Abbe's Sine Condition must be satisfied for high resolution and fidelity optical systems (a)Commercial systems satisfy the sine condition and do correction for single plane (b) Object rays with angle θ mapped to pupil plane.

From the formulation of Abbe's Sine Condition $\rho = sin(\theta)/sin(\alpha)$. In order to full fill the sine condition we can work with Fourier optics according to the following equation system:

$$\delta\phi(dz) = dz \times n \times k\sqrt{1 - (x_p^2 + y_p^2)/f_{obj}^2} \tag{2.4}$$

$$\delta\phi(dz) = dz \times n \times k\sqrt{1 - (x_p^2 + y_p^2)/f_{obj}^2} \tag{2.5}$$

$$\delta\phi_{m_x} = 2\pi \times (\delta x/d) \times m_x \tag{2.6}$$

$$\delta x(x_p, y_p) = d/2\pi \times dz \times n \times k\sqrt{1-(x_p^2+y_p^2)/f_{obj}^2}$$

$$\delta y(x_p, y_p) = N \times d/2\pi \times dz \times n \times k \qquad (2.7)$$

$$\sqrt{1-(x_p^2+y_p^2)/f_{obj}^2}$$

This allows us to introduce a constant focus step between successive image planes while countering the depth-induced spherical aberration that would normally follow from using the objective at the "wrong" focal plane.

2.4.2 Optical design of the original MFM system

Aberration-corrected multi-focus microscopy (MFM) implements aberration-free refocusing (as described in the previous section) by the use of diffractive Fourier optics. Diffractive Fourier optics allows complete control of the wavefront of the light transmitted through the optic, but in return requires correction of the chromatic dispersion introduced by the diffractive element. The components of the original MFM system is shown in Fig2.6 and consist of three custom elements and a system of two relay lenses which form a conjugate Fourier plane and a conjugate image plane.The Multifocus Grating (MFG) is placed in the Fourier plane to multiplex and refocus the image beam and is followed by the chromatic dispersion correction module which consists of a diffractive and a refractive element.

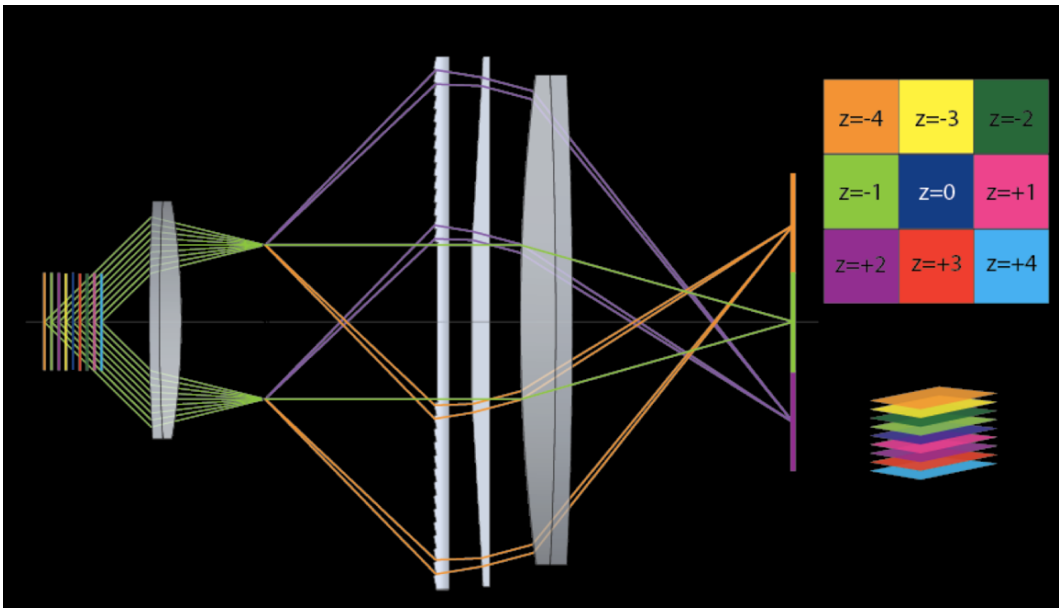

Figure 2.6: Classical Multifocus Microscopy System capable of capturing multiple planes into one detector. This system requires a Multifocus Grating (MFG) and a color-correcting module composed of blazed grating and multi-faceted prism. The MFG alone is capable of producing instantaneous focal stack in monochromatic light

Diffractive optics components can be made to multiplex light into beams with different relative intensities. Examples of diffractive gratings are line gratings and blazed gratings Fig2.7.

Figure 2.7: Diffractive optics elements (a) Line grating (b) Blazed grating

The multifocus grating function is designed by an iterative algorithm called the `'pixelflipper.m'` [1] to optimize even light intensity across the 3x3 or

5x5 target function as described in Appendix A.1.

The MFG is a phase grating which multiplexes the image beam and introduces a refocusing function as previously described in section 2.4.1. Due to the strongly dispersive nature of diffraction even a small change in wavelength results in a smear in the resulting image which must be corrected to avoid loss of resolution and peak intensity. The grating equation describes the variation in diffraction angle as a function of wavelength according to $a \cdot sin(\theta) = m \cdot \lambda$ where a is the grating period, θ is the diffraction angle and m is the diffraction order.

Even across the small bandwidth of the emission spectrum of a fluorophore ($\approx \Delta\lambda = 30nm$) dispersion would severely deteriorate image quality. To correct for this chromatic dispersion, the classic MFM systems use a blaze grating to counter the dispersion of the MFG and a multi-faceted prism to redirect the different beams to their proper positions in the focus stack array on the camera sensor Fig2.6.

Chapter 3

25-camera-array Multifocus Microscope (M25)

This chapter describes the optical design, diffractive optics nanofabrication, building, testing and application of the M25 instrument. In essence, M25 extends the imaging capacity of classical MFM instruments by utilizing a camera array as detector to capture deep image volumes at maximal speed. The new layout also includes a simplified chromatic dispersion correction system which will make the system easier to disseminate in other labs and in potential future commercialization of MFM technology.

3.1 Theory and Design

Classical MFM systems typically image either seven or nine simultaneous focal planes and have excellent performance in high-speed, high-resolution 3D imaging of smaller 3D volumes. Applications in biology include imaging of molecular signaling and transcription inside the cell nucleus and functional imaging of a subset of neurons within a neuronal network. Despite the possibility of using a diffractive optic to multiplex the image beam to an arbitrary number of planes, Multifocus microscopy has in biological imaging practically been limited to imaging a maximum of nine focal planes, since all planes were imaged onto a single camera sensor. Larger imaging volumes require a larger number of focal planes which cannot be imaged onto a single sensor without compromising sampling resolution. To extend the applicability of multifocus microscopy to larger sample volumes, we have redesigned the optical system to multiplex the image beams onto an array of detectors, here arranged in a 5x5 array to form 25 simultaneous focal planes. The design can be extended beyond these 25 planes by simply redesigning the grating function and including additional cameras.

This new optical layout importantly also enables a new chromatic dispersion correction design for diffractive multifocus optics. The chromatic dispersion correction module of classical MFM is somewhat complex in consisting of a combination of a custom made multifaceted prism and a diffractive grating,

limiting the feasibility to extend to more focal planes. The multifaceted prism was also prohibitively expensive and difficult to fabricate. M25 chromatic dispersion correction is elegantly simplified by implementing single individual blazed gratings mounted on each camera in the array. This new design thus enables us to capture larger imaging fields and opens up the door for a simplified and improved chromatic correction scheme that eliminates the need for the multi-faceted prism of the chromatic correction module.

M25 thus addresses previous limitations by employing an array of simultaneously acquiring, fast and tiny CMOS cameras Fig 3.7. The chromatic correction module contains no prism but only blazed gratings, mounted in the filter mount of each camera, and perfectly corrects chromatic dispersion across the entire color spectrum. M25 thus becomes a powerful instrument for deeper volume imaging and can be made from off-the-shelf optical components and home-made diffractive optics only. Here we demonstrate a prototype, ultrafast 25-camera-array multifocus microscope (M25) capable of imaging 25 focal planes at (130x130x50 μm^3).

3.2 M25 Grating Function Design

To design the multifocus grating function we have utilized the `pixelflipper.m` iterative algorithm [1] which allows us to generate a fan-out array with the proper intensity distribution to obtain even signal in all focal planes Fig 3.1.

Using the grating function in Fig 3.1, we obtain a theoretical transmission efficiency of 77% into the 5x5 array. This grating also takes into account part of central order m=0 and suppresses it to ≈ 96% to compensate for the ≈ 5% loss in the chromatic correction blazed gratings. The normalized theoretical grating efficiency is as follows:

$$\text{Amplitude } 5 \times 5 = \begin{bmatrix} 0.0310 & 0.0304 & 0.0306 & 0.0316 & 0.0307 \\ 0.0305 & 0.0307 & 0.0302 & 0.0311 & 0.0316 \\ 0.0306 & 0.0302 & 0.0297 & 0.0302 & 0.0306 \\ 0.0316 & 0.0311 & 0.0302 & 0.0307 & 0.0305 \\ 0.0307 & 0.0316 & 0.0306 & 0.0304 & 0.0310 \end{bmatrix}$$

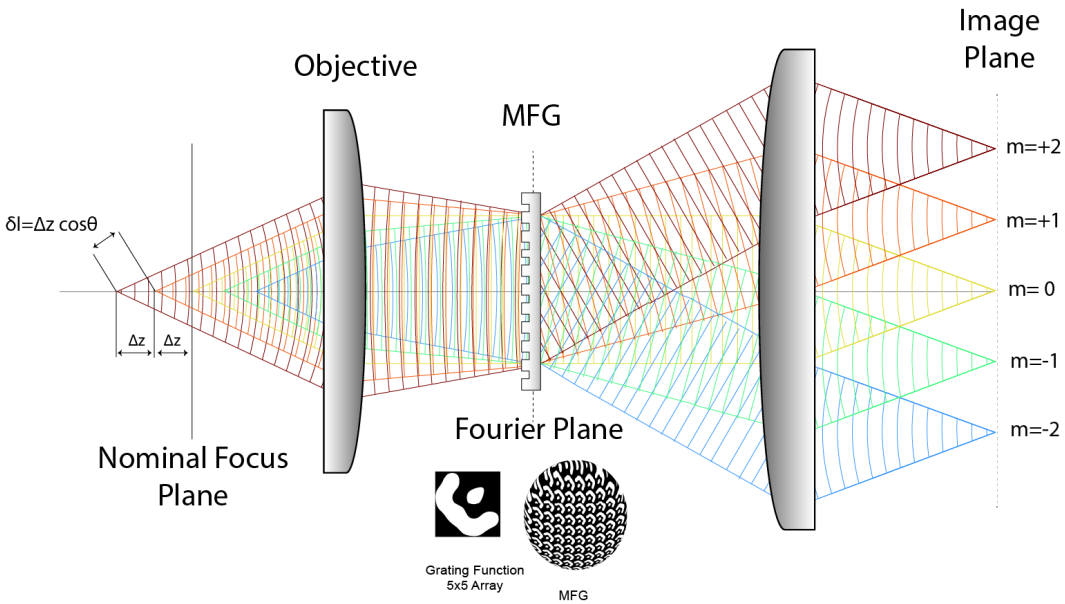

Figure 3.1: M25 refocus correction for aberration-free simultaneous imaging of 25 focal planes.

For the M25 MFGs we then apply eq2.7 functions to distort and create the focal shifts between the cameras in the array Fig3.1. For the M25, we use not

only the 1st diffraction order $m = \pm 1$ but the $m = \pm 2$. We simulated two M25 designs: one for the Marine Biological Laboratory (MBL) and another for the University of California Santa Cruz (UCSC). Both system were designed taking into account the specimen and FOV required for study. For the MBL system, we maximized the volumetric capturing capabilities by capturing 130x130x50 μm^3 voxels up to 50FPS Fig3.2, and for the UCSC M25 system, we prioritized *Drosophila* eggs, and *C.elegans* embryos for 50x50x50μm^3 for 100FPS Fig3.3.

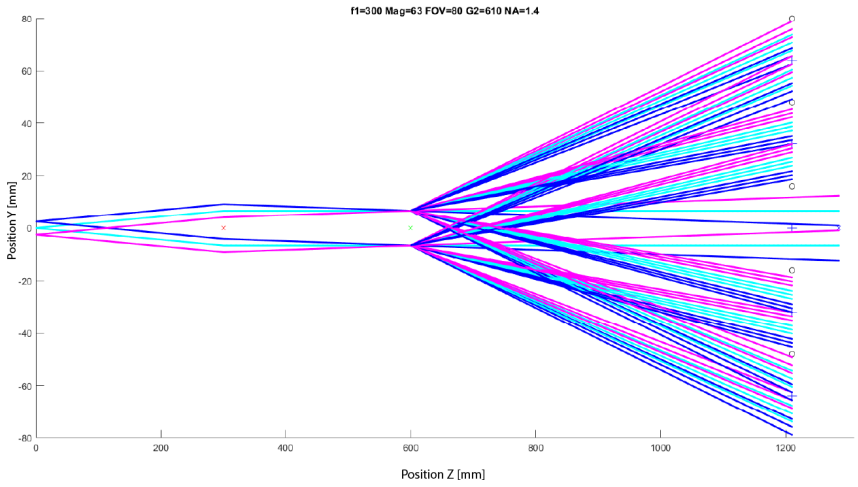

Figure 3.2: Optical Ray Tracing simulation for M25 for a 63x oil immersion objective 1.4NA for a FOV of 130x130x50μm^3. This system utilizes a relay lens f1=300mm noted by the red cross and the position of the MFG at green cross. The CCG position and separation between the camera array is noted by the circles were we can fill the CCG aperture and separate the orders with a 10μm MFG pattern period.

The ray-trace simulations start at the primary image plane located right at any commercial microscope's side port. The two M25 designs these simulations are done for a 50nm bandwidth based on the designed emission spectra. Both systems were designed for the same green fluorescence emission spectra ($\lambda =$

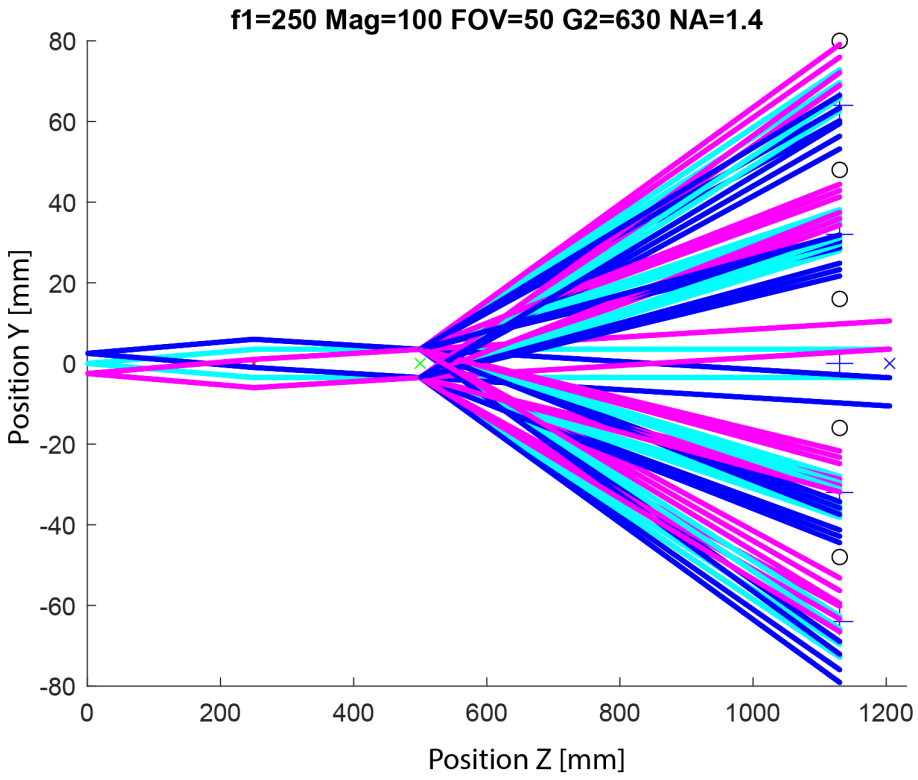

Figure 3.3: Optical Ray Tracing simulation for M25 for a 100x objective 1.35NA for a FOV of 50x50x50μm^3. This system uses a f1 relay lens f1=200mm (red cross) and MFG position (green cross) with pattern period 10μm. The CCG and 5x5 camera side-view are noted by the circles to ensure the orders are separated.

$500 - 530nm$) summarized in Table 3.2

3.3 Chromatic Dispersion Correction

The M25 system simplifies the classical MFM system by using a blazed grating mounted on a filter mount for each camera. This perfectly corrects for chromatic dispersion across the entire color spectrum, making it a powerful tool for deeper simultaneous volumetric imaging. As discussed previously,

the use of diffractive optics in our case the MFG introduces chromatic dispersion. One solution for the dispersion is to use narrow-band emission filters to have monochromatic light. This works well for label-free methods where we have more emission intensity, however, for the fluorescence case we would be throwing away those photons and the signal-to-noise ratio (SNR) would be low practically limiting the speed of acquisition. Hence, the development of these custom CCGs is key to MFM systems.

If left uncorrected, the chromatic dispersion for each axis would be following:

$$\delta x = \frac{mf\Delta\lambda}{d_x}, \delta y = \frac{mf\Delta\lambda}{d_y}, \delta z = \frac{\Delta\lambda}{\lambda_c} f_{m,n} \tag{3.1}$$

where m and n describe the horizontal and vertical position of the diffraction orders in the mxn=5x5 array.

3.4 Design and Nanofabrication of Diffractive Optics

The nanofabrication of custom diffractive optics in fused silica and quartz masks can be done at a open-academic nanofabcrication facility. The parts described in this paper were manufactured by hand and by the author at the UC Santa Barbara Nanofabrication Facility. The two custom diffractive optics nanofabricated were the MFG and the CCGs.

After the raytracing simulations and determining the f_1 lens focal length, we calculate for the pupil size, select the appropriate multifocus grating pattern, and generate the appropriate masks to cover the back focal plane of the objective in the Fourier Plane. For this system we tested two MFG patterns shown in Fig3.4 (a) and (b) with different m=0^{th} order suppression with 96% and 86%.

$$\begin{aligned} f_{obj} &= f_{TL}/M_{obj} \\ rp &= NA \cdot f_{obj} \\ MFG_{pupil} &= 2 \cdot rp \cdot (f_1/f_{TL}) \end{aligned} \tag{3.2}$$

The generated MFGs using equation 3.2 are then distorted for to generate the desired defocus correction and saved as `.bmp` files. In most cases, the files have to be chunked into 2 or 4 files due to the large size and the `.bmp` file format limitation of 4GB. These files can be loaded to GenISys Beamer Software utilized for electron and laser-beam lithography and stitched together to generate `.oas` or `.gds` files. These are standard formats for photolithography mask making and can be sent to photomasks makers for development. We can choose to print a couple of patterns in one 1x Quartz photomasks with the features or background in chrome. These 2.2mm thick masks can be diced into 17x17mm squares with MFG pattern centered as in Fig3.4(c).

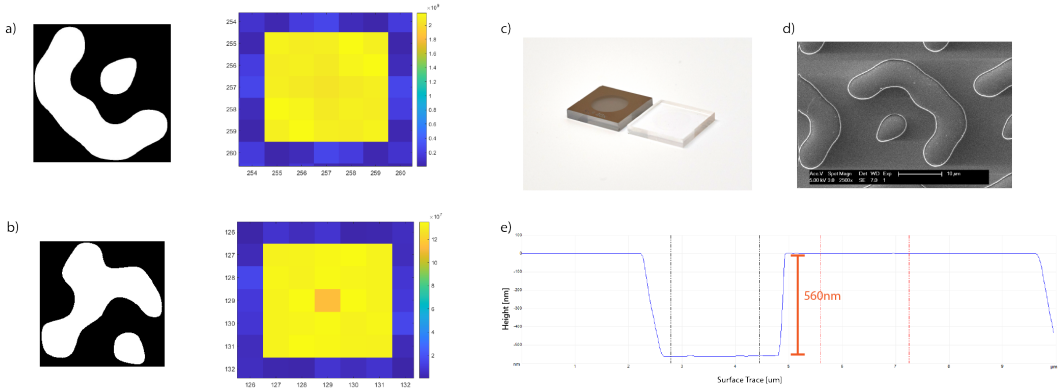

Figure 3.4: M25 MFG 5x5 Nanofabrication (a) M25 pattern with transmission efficiency of 77% and 0th order suppressed to 96%. (b) M25 pattern with transmission efficiency of 77% and 0th order suppressed to 86%. (c) Diced MFG with Chrome layer and pattern (left) π phase binary phase MFG with chrome mask removed (d) M25 grating function pattern under SEM to confirm etch depth and pattern existence (e) AFM results for M25 MFG dry etch. Precise, sharp walls, and smooth surface etching can be done on quartz photomasks to make custom diffractive optics with desired phase-shift

The grating pattern and efficiency simulation in Fig3.4(a-b) were optimized for π-phase shifts. This can be achieved in practice by etching the piece of quartz a depth $d = \lambda/(2 \cdot (n_1 - n_2))$ for n_1 equal to the refractive index of the material to be etched ,n_2 the refractive index of medium, λ designed wavelength. For the $\lambda = 515$nm and quartz n=1.46, the desired etch depth for a π-phase shift is d=560nm. For the nanofabrication, we focused on sharp and vertical walls and smooth surfaces to limit the loss of light due to scattering. To etch the square pieces containing the MFG, these were placed on a Si with SiO_2 carry wafer, and etched with the PlasmaTherm 770 ICP-SLR etcher.

Depending on the M25 setup design, different pupil sizes depending on the designed setup. With this specific etcher the power settings of 50/500W for

the coils, pressure at 5mTorr and a combination of $CHF_3 + O_2$ gas with flows of 30 and 15sccm respectively produced practically perfect smoothness. The MFG grating pattern size to etch ratio was about 0.033 $\mu m/s$ for the masks with $10\mu m$ feature size giving. These masks were measured with the AFM obtaining smooth surfaces with Ra = 0.4nm Rq=0.7nm. Figure 3.4 (e) shows the vertical walls, π etch depth and smooth surfaces.

CCGs were nanofabricated on 1mm thick 100mm diameter (Corsix A3852bsw) UV-Grade Fused Silica wafers through a one metal deposition step and a four step photolithography process. The first step was the 200nm layer of Chrome on one side of the wafer to create an opaque surface for the ASML 5500 stepper in order to be able to shoot the alignment marks. For all the patterning steps for photolithography of the fused silica wafers, a layer of DUV42P Bottom Antireflecting coating and UV6-0.8 Positive Resist were utilized. To create the chromatic dispersion blazed gratings, we approximated the blazed shape with an 8-step staircase of $\pi/8$ steps. Given the geometrical order of the diffractive orders as shown in Fig3.5(b) 5 different patterns were generated, which repeat around each quadrant. Although the CCG module can be skipped by placing a narrow band emission filter in the optical path, this severely limits the amount of light that can be possibly collected with our detectors. Instead, we can design custom chromatic correction gratings to optimize for the light transmission efficiency to perform fast, live, high-resolution 3D imaging.

For the 3 step photolithography process, given the geometry of the array with respect to the optical axis, 5 different CCGs patterns are required. For example, for CCG pattern 2 as shown in Fig 3.5 (b), the diagonal diffracting angle from the MFG is $\sqrt{x^2 + y^2}$

The photolithography process exposes masks A,B,C as noted in Table 3.1 with ASML Stepper and we use the same PlasmaTherm 770 ICP-SLR etcher dry etching method to do $\pi, \pi/2$, and $\pi/4$ etches into the fused silica wafers. This process is detailed in Fig3.5 to create the blazed structured pattern in the glass.

Mask ID	Pattern [nm] A	Pattern B [nm]	Pattern C [nm]
1	1250	2500	5000
2	884	1768	3536
3	625	1250	2500
4	559	1118	2236
5	442	884	1768
Etch depth [nm]	145	289	578

Table 3.1: CCG Patterns for all 5 different gratings for $10\mu m$ period MFG gratings with design wavelength of $\lambda = 532$nm. Pattern A, B, and C are shot alphanumerically and etched with its respective to achieve πphase shift

The pattern is shot on the wafers with 50% overlapping for evenness and alignment across layers covering about 70% of the wafers surface. From one CCG patterned wafer, we utilized a laser cutter doing low power fast small etches to cut out 4x29mm diameter circular CCGs per wafer Fig3.5 (d). For one complete M25 set, we require one wafer for pattern 1,2,3,5 and two wafers for pattern 4. These circular CCGs are cut to 29mm as this is the filter size

for the camera lenses utilized for both M25 builds, so we can easily attach the grating in front of the camera lens Fig 3.5 (c)

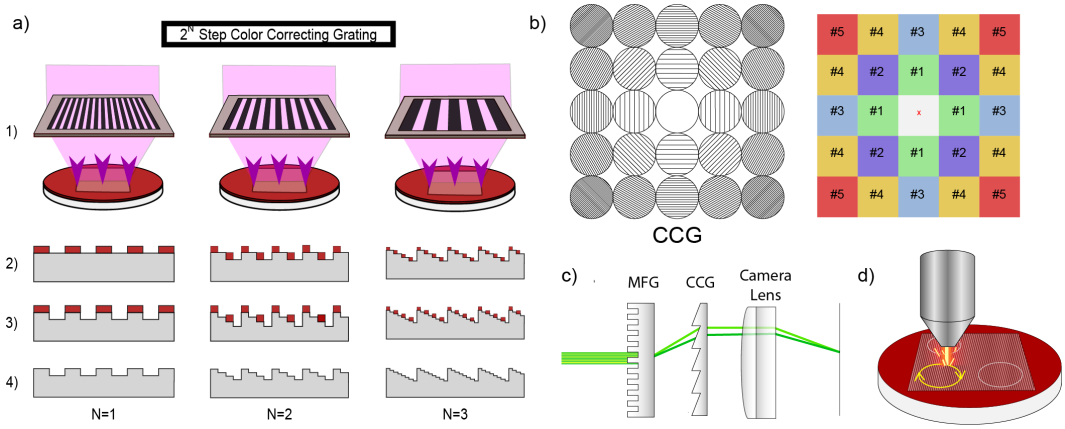

Figure 3.5: CCG Nanofabrication Process to create a complete set for the M25. (a) 3 step photolithography process to create an 8-step approximation of the blazed grating with theoretical transmission efficiency of $\approx 90\%$. (b) 5 different patterns required to correct for the chromatic dispersion. The 0th order does not require a grating as there is no dispersion in the optical axis. (c) Arrangement of the MFG, CCG and camera lens to demonstrate the M25 chromatic dispersion correction module (d) Laser cutting patterned CCG wafers to get 29mm circular gratings to be placed in standard camera lens filter holders.

3.5 M25 assembly

The M25 system was prototyped in two instruments at different imaging facilities: Marine Biological Laboratory in Woods Hole, MA and the University of California Santa Cruz Life Sciences Microscopy Center. Like the classical MFM system, the M25 is built using one of the side-ports of a commercial microscopy system Fig3.6 (c). This optical imaging system can be built with a pair of custom diffractive optics, MFG and CCGs, and off-the-shelf compo-

nents to capture high-resolution and ultra fast 3D imaging.

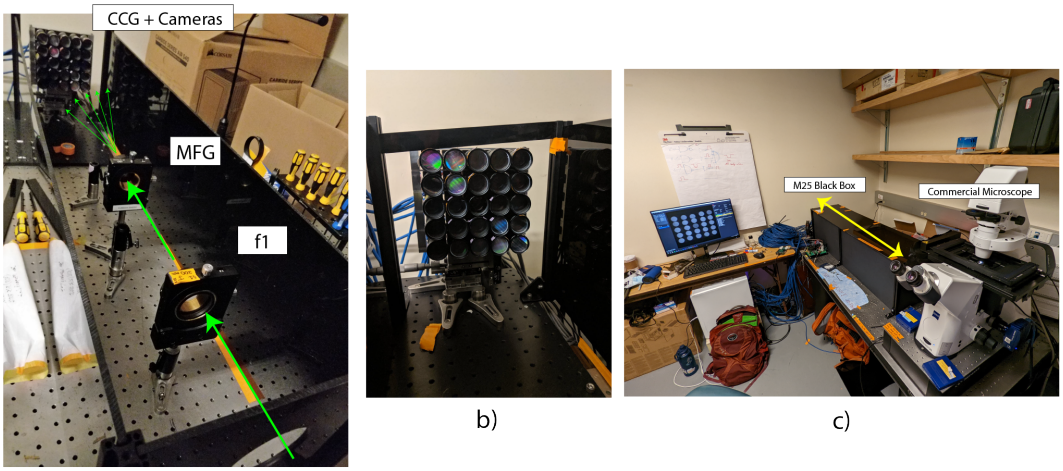

Figure 3.6: M25 system setup on side port of the camera. (a) Optical path of light coming out of the a commercial microscope side-port to get multiplex and refocused by the two pair of gratings. (b)5x5 camera array with corresponding CCG's placed in the lens holders. (c) System is placed on a black box for imaging and can easily be built on a side-port of a scope.

The M25 prototypes built were customized for different FOV and axial sampling to help answer specific biological questions. The M25 at the MBL focuses on imaging larger FOV of 130x130x50μm^3 for large neuronal imaging to the trade-off of lateral and axial sampling. Considering that the neurons both in *C.elegans* and *P.marinus* are larger than 2μm, the implementation has a total magnification of 15.8x using pixel sizes of 6um, for a slight undersampling. On the other hand, the system at UC Santa Cruz has a 1um or 2um Δz focus stepping between planes with an effective total magnification of 37.5 on 5.8μm pixels.

The following table 3.2 summarizes the two prototype builds of the M25.

	MBL System	UC Santa Cruz System
FOV [μm]	130x130	50x50
Δz [μm]	2	1 or 2
Total Volume [μm^3]	130x130x50	50x50x25 or 50x50x50
Speed [VPS]	50VPS	160VPS
Optimized Wavelength [nm]	515-532	515-532

Table 3.2: M25 Prototypes built at the Marine Biological Laboratory and the UC Santa Cruz imaging facilities.

For alignment of camera focus, we utilized an "alignment MFG" which multiplexes the beam without refocusing it. This component is extremely useful for the alignment of the M25 camera focus settings. While these are prime lenses (no magnification adjustment) they still have variable focus, and while this focus should be set to "infinity" to properly form an image when working as a tube lens, this "infinity" focus must be fine tuned so that all lenses in the array are imaged onto the same plane.

3.6 M25 Characterization

The M25 system was characterized by using Tetraspeck yellow-green 200nm fluorescent by imaging the bead across the whole imaging volume. This allows us to determine the actual separation between the focal planes and obtain the homography matrix to correct for the (x, y) displacement between the planes.

To confirm the focal stepping we designed the MFG for, we performed a Gaussian peak fit and took the maxima of the peaks at the best focus position per plane Fig3.8. The linear fit of the best focus positions confirms a $2\mu m$

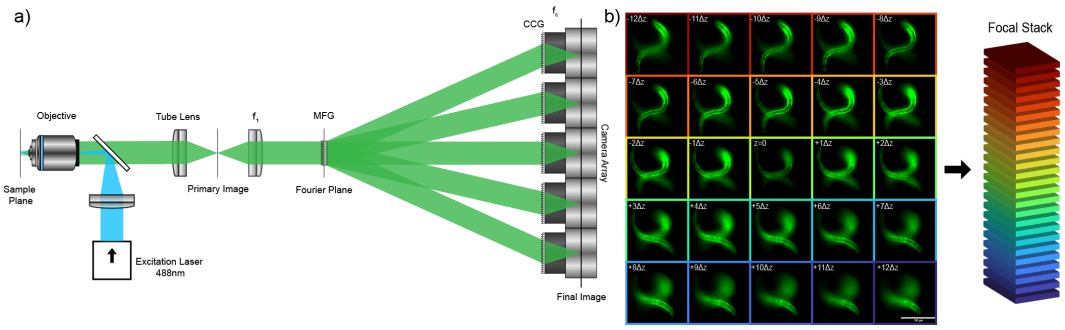

Figure 3.7: M25 Optical layout. (a) Wide-field fluorescence microscope with M25 attached on the side port. The system uses a f1 relay lens to place the MFG in the Fourier plane to diffract the light into the camera array. The camera array collects the beams as it hits the chromatic correction modules in tandem with the camera lenses. (b) 5x5 array of the M25 depicting the focal stepping across the array in order to collect the focal stack.

separation between the focal planes.

The bead dataset for characterization can be used by taking the maximum intensity projection per plane to determine the bead positions per plane to use computer vision algorithms to align the images axially. The alignment procedure was done by detecting the (x, y) shift of the cameras with respect to a camera in the array and stored in a `.csv` file. The calibration procedure should be in theory done once unless the system is re-aligned and this transformation matrix is applied on every dataset for reconstruction. M25 does not require major reconstruction algorithms aside this focal stack alignment procedure which is not computationally heavy as it is a simple affine matrix transform.

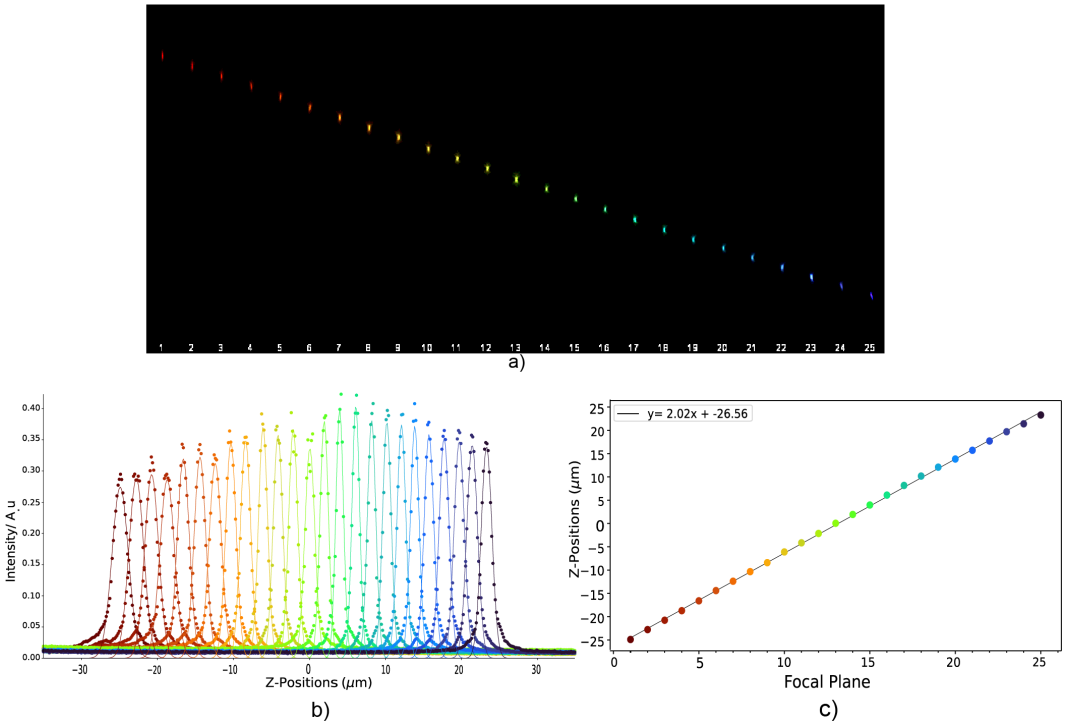

Figure 3.8: M25 PSF Stack analysis for all 25 planes on 200nm Tetraspeck yellow-green beads. (a) PSF xz montage display of aberration-free refocusing for each plane with $\Delta z = 2\mu m$(b) Gaussian peak fitting to the bead signal across a 70um volume.(c) Best focus position per plane based on Gaussian peak fitting maxima. The linear fit confirms the $\Delta z = 2\mu m$ focus step per plane. The focal planes are depth color coded using Turbo LUT.

Chapter 4

Imaging with M25

M25 opens the door for high temporal dynamics of neural circuits in freely moving organisms to process and understand multisensory information from single or multiple neurons [35]. In this chapter demonstrates the capabilities of the M25 by deploying it in several preliminary biological studies. We focus on the use of M25 for looking at fast and live-3D dynamics in lamprey (*P. marinus*),(fruit fly) *D. melanogaster*, *C.elegans*.

4.1 Imaging Experiments

4.1.1 Lamprey and Zebrafish neuronal imaging

In a pilot study to verify the resolution of the M25 instrument in deep 3D high-resolution imaging, we imaged the lamprey (*P. marinus*) spinal cord

motor neurons and the zebrafish (*D. rerio*) fin nervous system. For both samples, we cover the whole $50\mu m$ in depth were we can resolve a neuron cell body and axon Fig4.1(a) and the multiple neurons and dendrites Fig4.1(b).

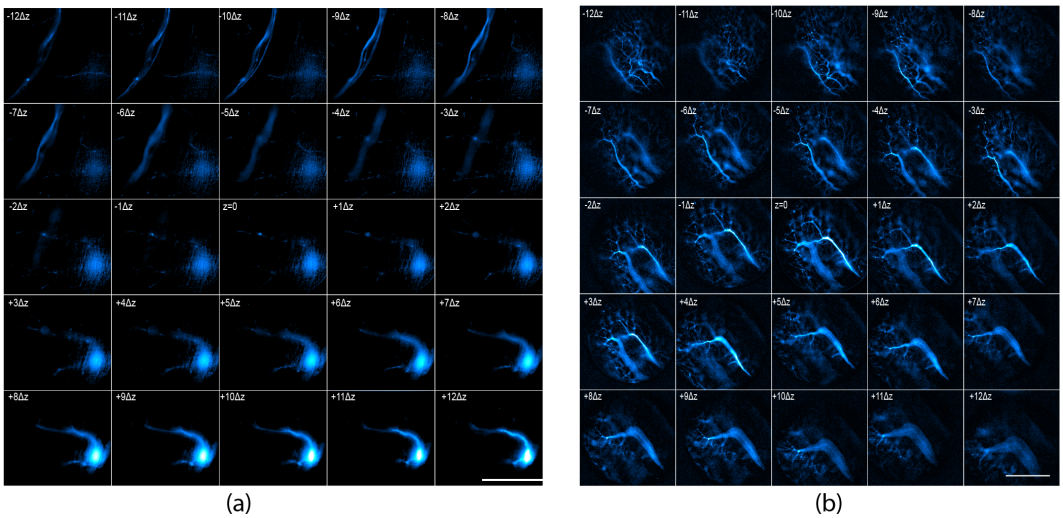

Figure 4.1: M25 Montage for lamprey and zebrafish. (a) *P.marinus* motor neurons 4 days post injection with 10kD Alexa 488 (b) Zebrafish nervous system near fin with GCaMP. Scale bar is $100\mu m$ LUT cyan hot

For the lamprey studies, we focused on imaging this large network of neurons along the spinal cord. We utilized Alexa 488 in 10kD and dissected 4 days post-injection for imaging to look at all the neural network Fig4.1 specifically focusing a the motor neurons and the connections to the spinal cord. This dye is very bright and allows visualization across all 25 planes at 30FPS. Additionally, we tested Calcium-green-1 dextran, an indicator of calcium signaling and presence in living tissues. Like Alexa 488 dye this dye was carefully injected in the lamprey spinal cord and imaged 2 days post injection. While we expect the M25 able to capture calcium presence in the neurons, no activity was ob-

served. In the future, further experiments with calcium indicators utilizing a perfusion pump with high potassium could help trigger and show the calcium influx and release.

4.1.2 Particle Diffusion Imaging

M25 can be used for measuring particle diffusivity and dynamics across a volume at high resolution and frame rate. We demonstrate this by tracking $1\mu m$ diameter fluorescent beads in water in a $50x50x50\mu m^3$ volume at 125FPS for 15 seconds Fig 4.2(a).

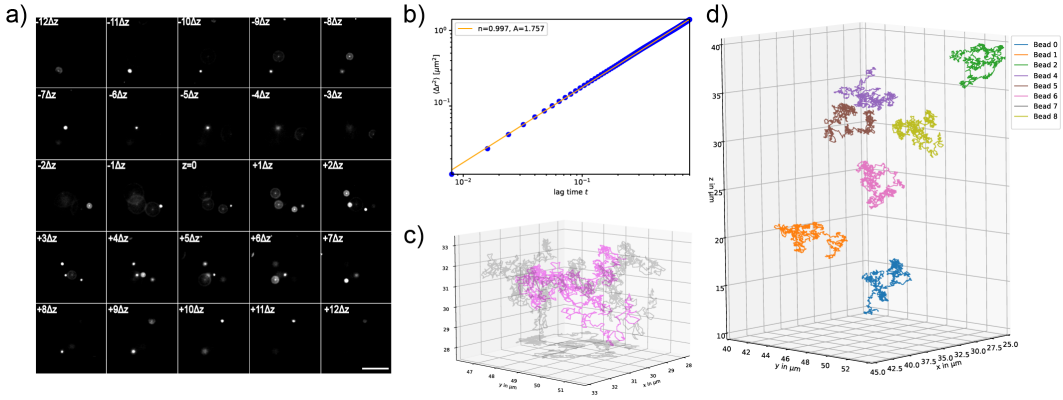

Figure 4.2: (a) M25 planes video montage capturing $1\mu m$ diameter fluorescent beads. (b) Diffusion Coefficient (c) Particle tracking for bead number 6 across time. (d) Particle tracking for 3D volume used for measuring the diffusion coefficient of nanoparticles in dionizied water. Scale Bar = $25\mu m$

Using particle tracking algorithms[36][37], we can determine the particles position in space across time Fig4.2(c-d) to measure the diffusivity constant of the spherical particles in the viscous material described by Stokes-Einstein Equation $D = \frac{k_B T}{6\pi\eta r}$ where k_B is Boltzmann's constant, T is temperature,η the

viscosity of water and r the radius of particles. To estimate the diffusivity of the particles, we use the collected tracks for all the particles to calculate the ensemble mean-squared-displacement (EMSD) of all the particles and fit the EMSD to the power-law At^n Fig 4.2 (b). For a viscous material like water,the expected power-law exponent $n = 1$ and obtained $n = 0.997$. The nominal value of $A = 4D = 1.728\mu m^2/s$ and we obtained $A = 1.757$ which is within 4% of the nominal value. [38].

4.1.3 Live Imaging of Drosophila Embryo in fluorescence and wide-field transmission mode

The first live test for the M25 was done on fruit fly (*Drosophila*) eggs, embryos and larvae. Although the eggs and embryo development are interesting and utilization of the M25, these do not exploit the fast and dynamic capabilities of this system. Here we show the beating heart valves of a drosophila larvae with GPF-H2 histones to look at cells across the whole organism labeled and dynamics. We here wish to point out advantage of the M25 wide-field imaging approach over other fast, and live 3D imaging techniques. By placing a narrow-band filter in the transmission path of the microscope, we can do label-free imaging of the sample to complement the information fro fluorescence imaging Fig 4.3[a-b]

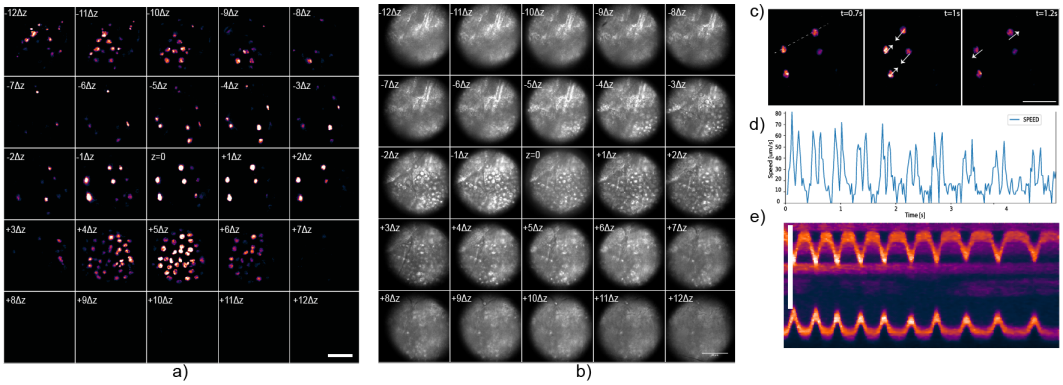

Figure 4.3: GFP-H2 on Drosophila larvae beating heart cells. (a) M25 montage of video of drosophila beating heart. Multiple layer of cells are captured across the volume (b) Bright field image of drosphila beating heart with the side walls show movement. (c) Selected timepoints depicting cells near valve beating at t=0.7, 1.0 and 1.2seconds.(d) Speed of beating cells tracked over time. (e) Kymograph of the fluorescence data across the line in (c). Scale bar is 25μm Using Gem LUT and appropriate image contrast enhancement.

4.2 Neuronal Signaling in Freely Moving *C.elegans*

The M25 fast 3D imaging allows the visualization and study of freely moving organisms to study their locomotion by capturing a volume were we can image young animals inside the FOV. Even if the animal swims outside of the nominal focus plane, the M25's simultaneous volumetric sampling allows one to track the worm in 3D. To demonstrate the capabilities of M25 system, we look at the coordinated movement of the *C.elegans* motor system that produces alternating contractions of antagonistic muscles along the body of the animal [39]. *C.elegans* have 95 body wall muscles staggered into two row each of 4 quadrants along the anterior-posterior axis. To produce a thrusting motion, this nematode uses a dorsoventral bending of the whole body that al-

lows the motions to be characterized as forward-motion, backward locomotion, dwelling and quiescence [40]. The forward-motion and activity of the motor neurons muscle-wall of the nematode are explored using the ZW495 [zwIs132 [myo-3p::GCamp2 + lin-15(+)] strain from the Caenohabditis Genetic Center of the University of Minnesota. This strain tracks the calcium activity along the muscle-body wall which allows us to track the activity with the M25.

The advantage of using the M25 is that we can place the worm in a non-viscous solution like water, to allow the worm to truly freely move instead of immobilizing or utilizing more viscous solutions to slow down and generate discontinuous locomotion. We used our customized python image processing pipeline to analyze the change of fluorescence in the body-wall muscle cells. For analysis, we track the position of the nematode using active contours and grayscale morphology to then use Skan to find the animal's skeleton [41] and interpolate the points along the muscle-body. To visualize and analyze the 3D volume we used and Napari for visualization[42]. Using the interpolated points of the skeleton, we projected perpendicular dorso-ventral regions-of-interest (ROI)s along the body-muscle to measure the calcium activity Fig 4.4b. For each frame we measured the summed the intensity of the 4 ROIS Fig 4.4c and then measured the fluorescence intensity of the top 80% pixels to prevent artifacts from hitting the edge of the animal or deformation of muscle. We then calculated the median of means $F_{80\%}(t)$ and normalized the time

series $\frac{\Delta F(t)}{F(t)}$. We plotted the traces of the $\frac{\Delta F(t)}{F(t)}$ of the animal fast undulatory frequency over time to demonstrate the forward locomotion in nematodes [43].

By studying the freely moving organism at high frame rate one can one could study activity patterns generated by different motor neurons at varying frequencies, [44] and utilize the calcium activity of the neurons and muscle cells to fill in existing computational models [45]

To demonstrate the capabilities for tracking and calcium imaging for neural circuits on freely-moving organisms we look at the *C.elegans* strain OH1625 [rab-3::NLS::GCaMP6s + arrd-4:NLS:::GCaMP6s] with bright paneuronal nuclear GCaMP6 expression from the Caenohabditis Genetic Center of the University of Mitinnesota. For this sample, we track the worm in 3D space and utilize TrackMate [37] to trace the neural activity over time for a selected number of neurons Fig 4.5 (a-c).

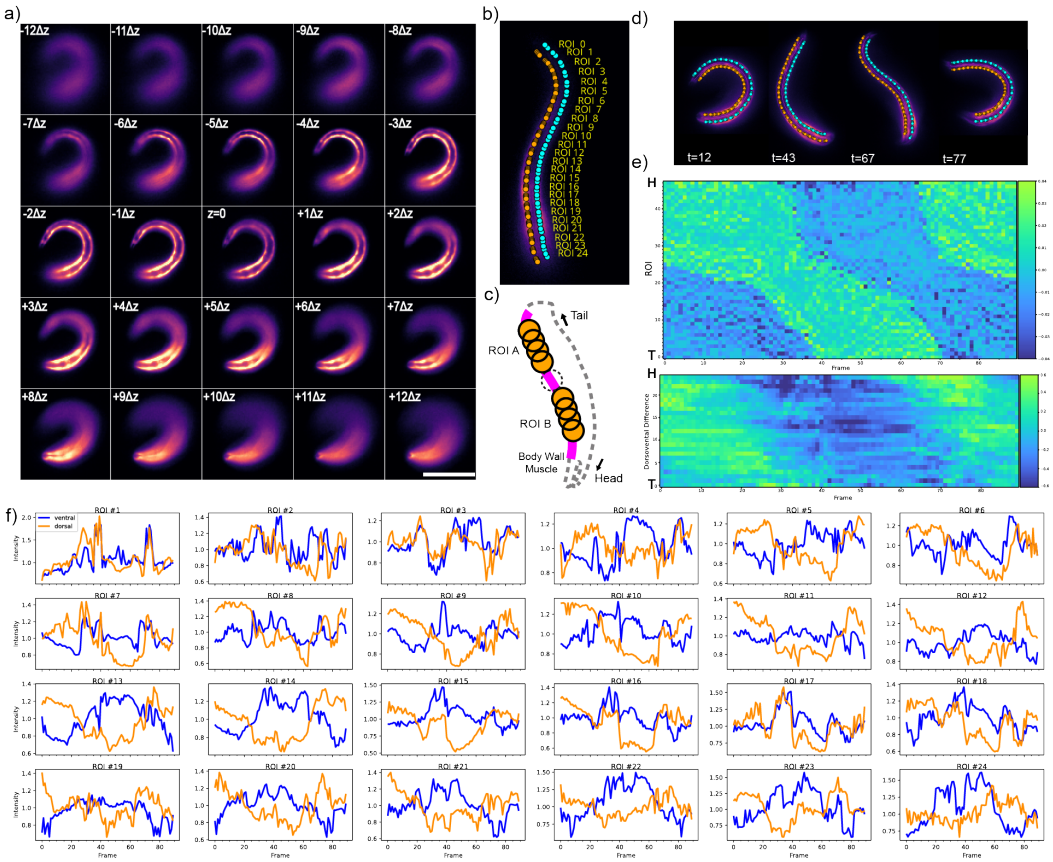

Figure 4.4: Multifocus microscopy tracking freely moving *C.elegans*.(a)5x5 array of *C.elegans* freely-moving (b) he ROIs for dorso-ventral measurements of muscle walls with NO.0 being the tail and NO.49 the head(c) ROI pattern consisting of 4 circular ROIs placed between the skeleton interpolated points while skipping one t (d) Pose of the worm undulation at frames $t = 12, 43, 67, 77$ acquired at 49FPS. (e) Green and Blue shaded areas in the kymograph represent the dorsoventral curvature where x-axis is the length of the animal from tail (T) at the origin and head (H) at the top along time (horizontal axis). Second plot shows the dorsoventral difference of $\Delta F/F$ sharing both x and y axis with curvature plot above. Colorbar is curvature Scale Bar = $70\mu m$

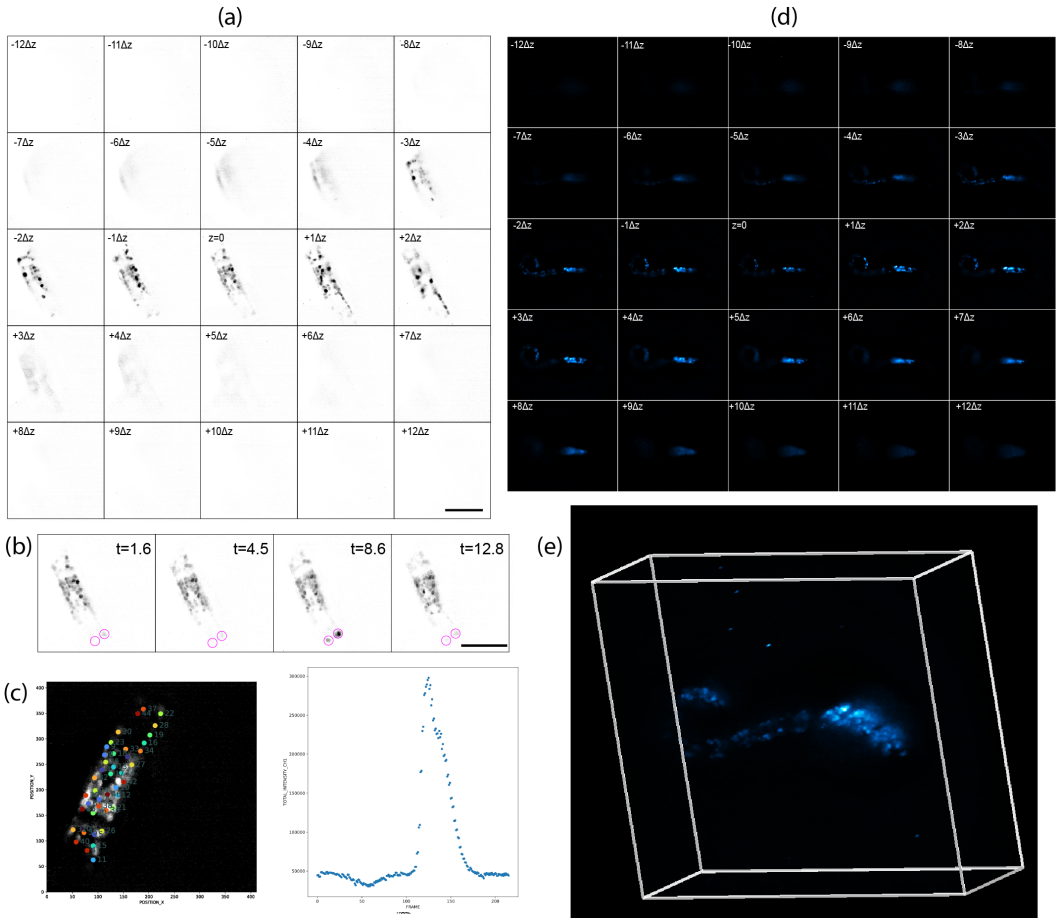

Figure 4.5: GCaMP 6 expressing paneuronal *C.elegans* L1-L2 size worms. Dataset 1 (a-d) (a) M25 5x5 array with nematode in focus across time. (b) Neural activity in tracked neural cells shown at t= 1.6,4.5,6.6, and 12.8 seconds.(c) Neural activity registered at colored dots and the neural activity from ROI 37. Dataset 2(d-e)(d)5x5 montage of camera array capturing freely-moving *C.elegans*. (e) 3D rendering of M25 array in (d). Scale bar is 25μm and the LUT is inverted grayscale for Dataset 1 and Cyan hot for Dataset2.

Chapter 5

User Friendly Acquisition

The following chapter describes the design of the acquisition pipeline used to capture the data from all 25 cameras simultaneously without drop of frames at 100Hz and the implementation of a graphical user interface (GUI) to allow the end user manipulate the M25 in a friendly and elegant manner.

5.1 Data Acquisition Pipeline

5.1.1 Acquisition Bottlenecks

The implementation of multiple cameras as detector for individual focal planes requires a custom acquisition engine and pipeline to effectively offload the images from all 25 cameras without drop of frames in a coordinated and synchronized manner. Currently, commonly used microscopy software, Mi-

cromanager [46], cannot effectively handle more than 2 cameras at >100FPS without dropping frames. Hence, we built a custom acquisition pipeline composed of 3 major components: the acquisition engine, timing controller board, and the Graphical User Interface (GUI) Fig 5.1.

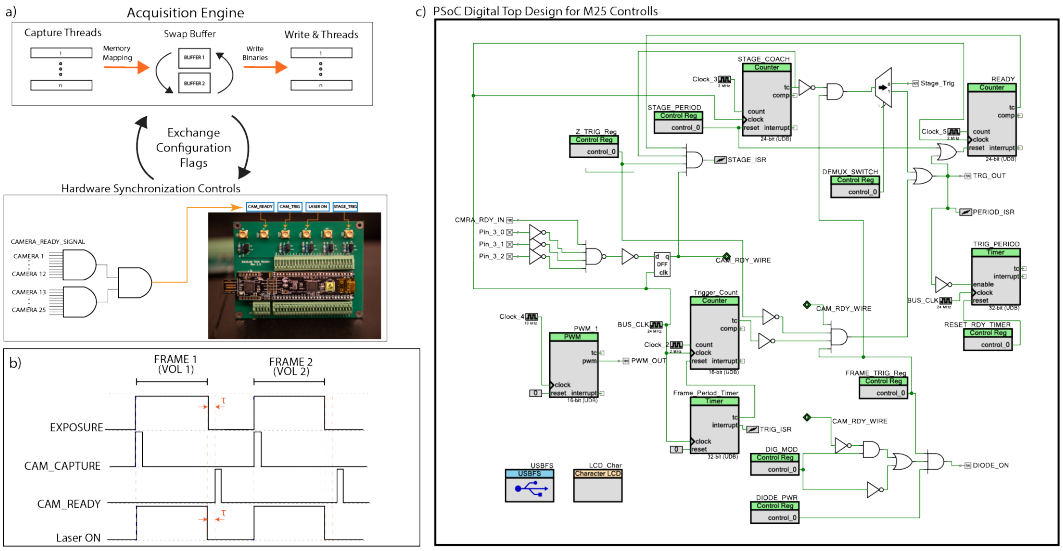

Figure 5.1: M25 Acquisition Pipeline (a) Diagram of the acquisition engine and timing control (b) Timing diagram explaining hardware synchronization of M25 cameras and additional optoelectronic hardware (c) Timing control digital logic for controlling stages,lasers and cameras

The acquisition engine was implemented with the goal of simultaneously capturing with all 25 cameras at 100FPS without drop of frames. This translates to simultaneously offloading 2.3 megapixel sensor with bit depth of 8-bits per pixel at 100FPS which is about $\approx$ 5.76GB/s for the whole array or 230MB/s per camera. Based of up-to-date off-the-shelf components for computing power, the main bottlenecks limiting the fast data offloading from the cameras to computer without loss of frames originate from two components:

the camera hardware and the memory used for storage. Currently, most CMOS cameras like the Basler 1920-155um utilized in the M25 utilize USB 3.0. as primary communication for data transfer. This causes the first bottle neck maximizing data transfer to 600MB/s per host controller in an ideal scenario. Therefore, the data throughput has to first be maximized through hardware by utilizing as many host controllers connected through PCIe cards to motherboard. In many cases, including the M25 computer build, one host controller can be shared between two camera devices if there are not enough individual host controllers. To maximize the throughput, we utilize 6 PCIe cards with 4 host controllers per card to have 1:1 host to camera pairs. The last missing camera is then connected directly to USB controller in the motherboard existing ports.

The second data bottleneck is writing and saving to disk. In this setup, we utilized a RAID0 array of NVME SSDs bench-marked at $\approx$ 6.6GB/s for sequential write to disk. Taking these bottlenecks into account, we optimized the parameters for imaging system by reducing the sensor size to 808x608 pixels to increase the pixel bit depth to 16-bits and enable acquisitions up to 160FPS. The M25 acquisition pipeline was consistently able to acquire $\approx$ 6.5GB/s to disk without drop of frames running at theoretically the maximum speed of the cameras.

5.1.2 Data Handling and Storage

Data handling and saving to memory as fast as the hardware allows is essential for the M25 saving system as delays in offloading data from the cameras can limit the maximum data throughput. Aside from the sensor readout speed, the system should not encounter major delays when writing. This is achieved by writing raw image data directly into a RAM swap buffer to then writing the RAM buffer directly to disk as a binary file. Post acquisition the binary files are converted into desired image format (i.e `.raw`, `.tif`,`.zarr`).

The M25 is uses a Windows 10 OS, so we implemented the file handling using the *Windows SDK File Handler* library for rapid storage into the NVME SSD Raid 0 array. As the NVME SSD Raid 0 is partitioned in 512B sectors, one fast method is by allocating buffers aligned for 512B sector offsets. The buffer size is equal to the camera number times the image size summed with 512 - (image size % 512) so we can perform pointer arithmetic and memory copy to pre-allocated memory locations.

As shown in Fig5.1, we directly write buffers to drive using 512B sector alignment for fast writing by bypassing the read and right functions default buffering with a pre-allocated memory aligned to the file-system offsets. Aligning the buffers in a 512B enhances the write speed as it one can do direct disk writing to known locations doing pointer arithmetic. We create individual acquisition threads for each camera and copy the sensor data into a location in

the sector aligned buffer. Each camera write thread points to an offset calculated by the image size and camera number in the array to allow fast memory copying without corrupting the data. Additionally, each camera thread has a synchronization point barrier-mutex to avoid racing conditions. For simultaneous reading from cameras and storing the binary files, we utilize two buffers as ping-pong or swap buffers that dynamically swap every time we acquire one second of data (for frame rates 1 frame per second and greater).

One caveat for using these dynamic swap buffers, is that we need to keep track of the number of frames written to prevent the acquisition from infinitely running. To know the end of acquisition, we keep track of the number of buffers written which is provided to the program given the camera configuration and frame rate. The algorithm acquires images and writes binary files until conclusion function notifies the acquisition threads to halt. Once the total number of frames desired are captured, the final data handling and storage is done by converting the binary files into the desired file format. For the M25, we chose to chunk the binary and convert to '.raw'. The multi-threaded conversion make individual folder for each camera and organizes the saving structure as:

```
AcquisitionFolderName
├─ CAM01
│  ├─ img001.raw
│  └─ img002.raw
├─ ...
└─ CAM25
   ├─ img001.raw
   └─ img002.raw
```

This file format can easily be loaded to common image processing tools such as `ImageJ`, python or `Matlab` by knowing the acquisition image size and bit depth. For our image processing pipelines, we read the `.raw` file format through our python image processing pipeline for image registration can calibration to then be saved as `.tif` or `.zarr` (See appendix for image processing code)

5.2 GUI and Napari

Instead of a Command Line Interface(CLI) application, which can be intimidating to users unfamiliar with such terminal windows, we implemented a user-friendly graphical user interface (GUI) as a Napari plugin [42] for easy deployment. Napari is a user friendly OpenGL based multidimensional data viewer that can be interface through python. As discussed above, since the M25 datasets can easily be parsed and loaded through python, we can utilize

Napari as main GUI by taking the advantage of both the multidimensional viewer and easy transferring of data. Additionally, as the data is loaded into python, we can utilize image processing libraries such as `OpenCV,scipy.ndimage,sckit-image, te` to perform all sorts of analysis as performed with the biological data imaging.

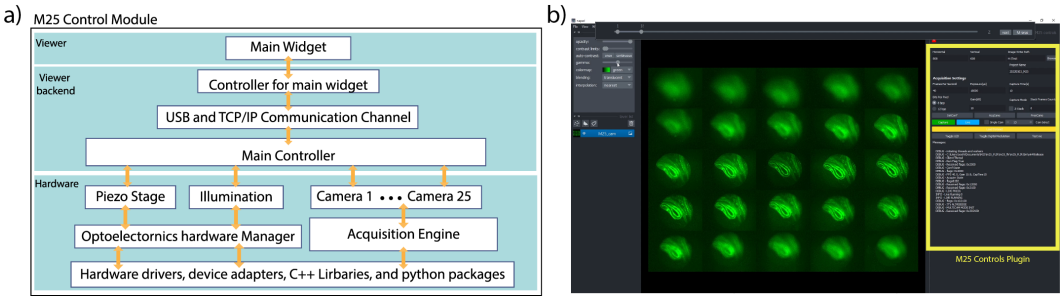

Figure 5.2: M25 Software and Hardware Architecture (a) Pyramid for M25 components (b) M25 Napari GUI Plugin for handling acquisition

5.2.1 GUI to Acquisition Pipeline Communication Interface

As shown in Figure 5.2(a) we utilized the Napari plugin as `Main Widget` which is the layer the user sees while opening the plugin in Napari. This PyQT5 based widget allows the user input the acquisition parameters(i.e file saving acquisition session name), and the acquisition settings(i.e camera exposure, frame rate, bit-depth,gain, and capture time), whose values are used to coordinate the M25 image acquisition.

The interface between the C++ code and the python GUI is established by adding two additional threads for communication. The first thread is a

TCP/IP thread that allows us to send send the information between python and C++ parsed in a predefined `struct` for easy encoding and decoding. The `struct` contains the GUI set acquisition parameters and settings which are essential pieces of information to modify the timing controls for synchronization.

5.2.2 Timing Control Board

The timing control board or `Main Controller` in Fig 5.2(a) is a PSoC 5 micro-controller for which we can program different digital blocks and logic to allow for precise timing control for hardware synchronization Fig5.1. This PSoC micro-controller has multiple input and output connections to the cameras, laser, stage and capabilities to control any other opto-electronics such as Spatial Light Modulators (SLM), shutters, and turrets. The main function of the PSoC is to send trigger signals to the multiple devices based of the information provided by the GUI. These parameters are mainly the exposure time, framerate and capture time, to adjust the timing clocks for precise and real-time controlled acquisitions which first send through TCP/IP between GUI and C++ program, decoded in C++ and sent through USB using `libusb` to the PSoC. To control most opto-electronic hardware, we can use Micromanager to configure the parameters for digital or analog triggering and control for PSoC to take over.

Chapter 6

Outlook

6.1 Future Directions

6.1.1 Faster Calcium Probes

In the future, the development of sensitive and fast voltage sensors would be the key as techniques like the one proposed in this thesis will require to study fast neuronal kinetics . As imaging technology gets faster,deeper and sensitive, the improvement of current dyes stability, fluorescence intensity and speed will allow us to answer biological questions in greater detail.

6.1.2 Label-free and Super Resolution

The simplification of the optical path for the M25 over the classical MFM systems allows for faster, deeper and larger live-3D imaging. The custom nano-

fabrication of diffractive optics allow for sensitive, fast and high-resolution 3D imaging for wide-field or biological organisms and their dynamics. By simultaneously capturing multiple volumes, the real limit of this technique is the total intensity from the sample and the camera capturing frame rate. For fluorescence microscopy, this limitation would be posed by the photo-toxicity, photo-stability and fluorophore intensity. However, this technique would be effective for label-free technique to measure the contrast of semi-transparent biological organisms such as bright-field, dark-field, polarization, phase contrast [[47], [24]]. Additionally MFM systems can be adapted for super-resolution imaging speeding up the acquisition of 3D volume [2]

6.1.3 Optical Sectioning

Ideal multifocus microscopy will require optical sectioning and background rejection with confocal-like resolution. Two methods that can be utilized to generate optically sectioned 3D images at the speed of light-sheet would be the implementation or addition of oblique plane illumination (OPM)[13] or utilizing the 3D Structured illuminating pattern can be a solution to this problem.

6.2 Conclusions

This work demonstrates the development of a new and simplified multifocus microscopy (MFM) imaging system pushing the depth, sensitivity and speed of acquisition to perform fast, live and high-resolution 3D imaging. The M25 demonstrates the capabilities to simultaneously capture multiple focal planes enabling the detection of fast biological dynamics such as neural activity and locomotion on freely moving organisms.

Our M25 system addresses previous limitations by employing an array of simultaneously acquiring, fast and tiny CMOS cameras. This optical layout also allows us to drastically simplify the chromatic correction module which here contains only a blazed grating, mounted in the filter mount of each camera, which perfectly corrects chromatic dispersion across the entire color spectrum. M25 thus becomes a powerful instrument for deeper volume imaging and can be made from off-the-shelf optical components and home-made diffractive optics only. Here we demonstrate a prototype, ultra-fast 25-camera-array multifocus microscope (M25) capable of imaging 25 focal planes at (130x130x50 um).

Appendix A

Simulation and M25 Control Code

A.1 M25 Simulation Code

Edited Sara Abrahamsson's original raytracer for faster implementation

```
clear all
clc
tic

%Edited from Sara's Ray Tracer to run faster 2019
%Grating & pixel measurement in microns (um)
%Your parameters for system and objective:
M_obj = 100;
NA = 1.4;
f_TL = 180; %tube length is 180 for olympus, 165 for zeiss (??? check!),↙
200 for leica and nikon
f1 = 250; %first intermediate lens (after tube, lens before secondary↙
pupil plane)
fc = 75; %second (last) intermediate lens, forms image onto camera
fov = 50
im_fov = 0.5*fov*(1e-3); %FOV
pixelsize = 5.8e-3
G12 =630;  %adjust to get to center of cameras G12 distance
%Calculated hardware properties
f_obj = f_TL / M_obj; %focal lenght of objective (not the same as wd)
d_pupil_obj = 2*NA*f_TL/M_obj; %size of pupil in objective
rp= NA *f_obj;
int_im_fov = M_obj*im_fov;
v_pRay_obj = im_fov/f_obj;%angle of rays from peripheral fov point when↙
exiting objective
d_G1 = d_pupil_obj*(f1/f_TL) %diameter of G1
Mtot = M_obj*(fc/f1)      %Total Magnification
pixSampling = pixelsize/Mtot

%Fabrication parameters
dg1 = 10e-3;

%Design wavelengths
%Using Green 500-550
l_min = 500e-6;
l_max = 550e-6;
l_med = (l_min+l_max)/2;
wav =[l_min l_med l_max];

%Distance CCG to G1
```

```
v_fov_int_im = int_im_fov / f1;

%Position
G2_pos = (2*f1+G12);
fc_pos=G2_pos+fc;   %size of the length of setup and size of lens fc ***↙
EDUARDO CORRECT

figure()
hold on
panel = 32; %Camera array separation in mm
n = 5;      %side of cam array (M25) 5x5
cam_boundary = zeros(5,1);
cam_center = zeros(5,1);
for i = -2:1:2
    cam_boundary(i+3) = panel/2 + panel*i;
    cam_center(i+3) = i*panel;
end
%Plot the boundary of cameras and the center of CCG
plot(G2_pos,cam_boundary,'ko');
plot(G2_pos, cam_center,'b+','MarkerSize',10);
plot(f1,0,'xr'),plot(2*f1,0,'xg'), plot(fc_pos,0,'xb')

%Functions
angle = @(rise,run) rise/run;   %Slope
y_ray = @(c,fov,x,slope)  (c * fov + x * slope);    %Equation of Ray

%Int_img to f1
angle_int= angle(rp , f_TL);
% int_ray = zeros(f1,6);
int_ray = ones(G12,6)*(2*f1+1);
x_f1 = 1:1:f1;
% %Trace from Secondary Image Plane to f1
for x = 1:f1
    int_ray(x,1) = y_ray(0,int_im_fov,x,angle_int);
    int_ray(x,2) = y_ray(0,int_im_fov,-x,angle_int);
    int_ray(x,3) = y_ray(1,int_im_fov,x,angle_int);
    int_ray(x,4) = y_ray(1,int_im_fov,-x,angle_int);
    int_ray(x,5) = y_ray(1,-int_im_fov,x,angle_int);
    int_ray(x,6) = y_ray(1,-int_im_fov,-x,angle_int);
end
%Plot from int_img to f1
```

```
% h = plot(x_f1,int_ray);
% set(h(1:2),'Color','b');
% set(h(3:4),'Color','r');
% set(h(5:6),'Color','g');

angle_f1= angle(int_im_fov , f1);
f1_g1_ray = zeros(fc_pos-f1,6);

% y_ray = @(c,fov,x,slope)  (c * fov + x * slope);
% Trace from f1 to G1
for x = (f1+1):(fc_pos)
    int_ray(x,1) = y_ray(1,int_ray(f1,1),-x+f1,0);
    int_ray(x,2) = y_ray(1,int_ray(f1,2),-x+f1,0);
    int_ray(x,3) = y_ray(1,int_ray(f1,3),-x+f1,angle_f1);
    int_ray(x,4) = y_ray(1,int_ray(f1,4),-x+f1,angle_f1);
    int_ray(x,5) = y_ray(-1,-int_ray(f1,5),x-f1,angle_f1);
    int_ray(x,6) = y_ray(-1,-int_ray(f1,6),x-f1,angle_f1);
end
size(int_ray)
x_fc= 1:1:fc_pos;
% size(x_f1_fc)
% size(f1_g1_ray)
h = plot(x_fc, int_ray,'.');
set(h(1:2),'Color','c');
set(h(3:4),'Color','b');
set(h(5:6),'Color','m');

%Trace from fc to camera

%Trace from G1 to G12
 %grating G1 (pupil plane, x = 2*f1) for rays from central fov point
%  wav_arr = ones(G2_pos+100,24)*(2*f1+1);    %24 since second order for↙
3 rays (center, peripheral up,down)
diffr_ray=ones(G2_pos-2*f1,24)*(2*f1+1);
 for i = 1:length(wav)
    lambda = wav(i);
    %grating G1 (pupil plane, x = 2*f1) for rays from central fov point
    y_cRay_m1_g1 = int_ray(2*f1,1);
    y_cRay_m1_g1_d = int_ray(2*f1,2);
    y_cRay_m2_g1 = int_ray(2*f1,1);
    y_cRay_m2_g1_d = int_ray(2*f1,2);
```

```
    %For m=1 and m=2
    angle_cRay_m1_g1 = lambda/dg1;
    angle_cRay_m2_g1 = 2*lambda/dg1;

    %grating G1 (pupil plane, x = 2*f1) rays from peripheral fov points
    y_pRay_m1_g1 = int_ray(2*f1,3);
    y_pRay_m1_g1_d = int_ray(2*f1,4);
    y_pRay_m2_g1 = int_ray(2*f1,3);
    y_pRay_m2_g1_d = int_ray(2*f1,4);


    angle_pRay_m1_g1 = lambda/dg1 + int_im_fov/f1;
    angle_pRay_m2_g1 = 2*lambda/dg1 + int_im_fov/f1;

    angle_pRay_m1_g1_dd = lambda/dg1 - int_im_fov/f1;
    angle_pRay_m2_g1_dd = 2*lambda/dg1 - int_im_fov/f1;

    for x = (2*f1+1):(G2_pos)
        %Center Ray m=1 & m=2
        diffr_ray(x-(2*f1),1) =y_ray(1,y_cRay_m1_g1,(x-2*f1),↙
angle_cRay_m1_g1);
        diffr_ray(x-(2*f1),2) = -1*diffr_ray(x-(2*f1),1);
        diffr_ray(x-(2*f1),3) =y_ray(-1,y_cRay_m1_g1,(x-2*f1),↙
angle_cRay_m1_g1);
        diffr_ray(x-(2*f1),4) = -1*diffr_ray(x-(2*f1),3);

        diffr_ray(x-(2*f1),5) = y_ray(1,y_cRay_m1_g1,(x-2*f1),↙
angle_cRay_m2_g1);
        diffr_ray(x-(2*f1),6) = -1*diffr_ray(x-(2*f1),5);
        diffr_ray(x-(2*f1),7) = y_ray(-1,y_cRay_m1_g1,(x-2*f1),↙
angle_cRay_m2_g1);
        diffr_ray(x-(2*f1),8) = -1*diffr_ray(x-(2*f1),7);

        %Peripheral Rays m=1 & m=2 Up
        diffr_ray(x-(2*f1),10) = y_ray(1,y_pRay_m1_g1, (x-2*f1),↙
angle_pRay_m1_g1);
        diffr_ray(x-(2*f1),9) = -1*(diffr_ray(x-(2*f1),10));
        diffr_ray(x-(2*f1),12) = y_ray(-1,y_pRay_m1_g1, (x-2*f1),↙
angle_pRay_m1_g1);
        diffr_ray(x-(2*f1),11) = -1*(diffr_ray(x-(2*f1),12));
```

```
        diffr_ray(x-(2*f1),14) = y_ray(1,y_pRay_m1_g1, (x-2*f1),↙
angle_pRay_m2_g1);
        diffr_ray(x-(2*f1),13) = -1*(diffr_ray(x-(2*f1),14));
        diffr_ray(x-(2*f1),16) = y_ray(-1,y_pRay_m1_g1, (x-2*f1),↙
angle_pRay_m2_g1);
        diffr_ray(x-(2*f1),15) = -1*(diffr_ray(x-(2*f1),16));

        %Peripheral Ray m=1 & m=2 down
        diffr_ray(x-(2*f1),17) = y_ray(1,y_pRay_m1_g1,(x-2*f1),↙
angle_pRay_m1_g1_dd);
        diffr_ray(x-(2*f1),18) = -1*(diffr_ray(x-(2*f1),17));
        diffr_ray(x-(2*f1),19) = y_ray(-1,y_pRay_m1_g1,(x-2*f1),↙
angle_pRay_m1_g1_dd);
        diffr_ray(x-(2*f1),20) = -1*(diffr_ray(x-(2*f1),19));

        diffr_ray(x-(2*f1),21) = y_ray(1,y_pRay_m1_g1,(x-2*f1),↙
angle_pRay_m2_g1_dd);
        diffr_ray(x-(2*f1),22) = -1*diffr_ray(x-(2*f1),21);
        diffr_ray(x-(2*f1),23) = y_ray(-1,y_pRay_m1_g1,(x-2*f1),↙
angle_pRay_m2_g1_dd);
        diffr_ray(x-(2*f1),24) = -1*diffr_ray(x-(2*f1),23);

        wav_arr(:,:,i) = diffr_ray;
    end
    x_fc= (2*f1+1):1:G2_pos;
    h= plot(x_fc,wav_arr(:,:,i),'.');
    title(['f1=' num2str(f1) ' Mag=' num2str(M_obj)  ' FOV=' num2str↙
(fov) ' G2=' num2str(G12) ' NA=' num2str(NA)])
    set(h(1:8),'Color','c');
    for j =9:1:24
        if(rem(j,2)==0)
        set(h(j),'Color','m');
        else
        set(h(j),'Color','b');
        end
    end
 end
% diffr_ray(G2_pos-(2*f1),:)

% x_fc= 1:1:G2_pos+100;
```

```
% size(int_ray)
% size(x_fc)
% h = plot(x_fc, int_ray);
% set(h(1:2),'Color','k');
% set(h(3:4),'Color','k');
% set(h(5:6),'Color','k');
% set(h(7:8),'Color','k');
% set(h(9:10),'Color','k');
% set(h(11:12),'Color','k');
xlim([0 G2_pos+100])
xlabel('X Optical Path  [mm]')
ylabel('Y Optical Path [mm]')

toc
```

A.2 M25 Napari Plugin

`https://github.com/SaraLab-Group/m25-napari`

A.3 M25 Acquisition Engine and Timing Control Code

`https://github.com/SaraLab-Group/M25_basler`

A.4 Extra Figures

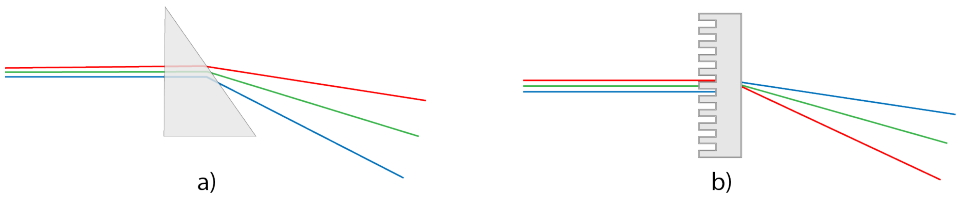

Figure A.1: Chromatic Dispersion by (a)Prism vs (b) Diffraction Grating

Appendix B

CAD Drawings

B.1 Camera Array Stand

Designed by Gustav Petterson and Eduardo Hirata Miyasaki

ITEM	DESCRIPTION	QUANTITY
1	Base plate	1
2	Camera plate	5
3	Spacer	10
4	Top plate	1

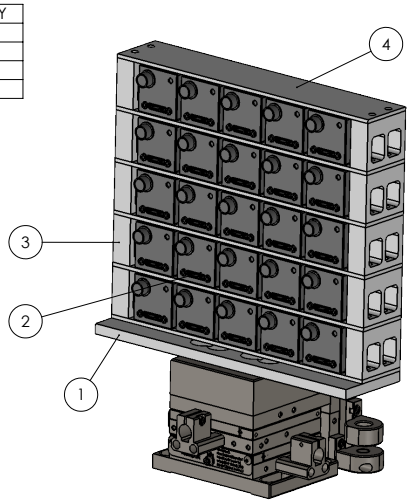

M25 camera array
Scale 1:2, Rev A

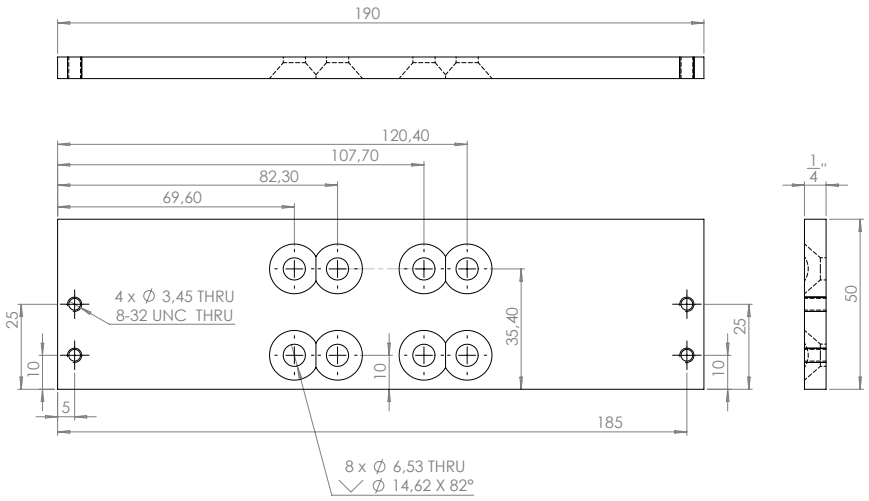

Base plate
Scale 1:1, Rev A
Units in mm

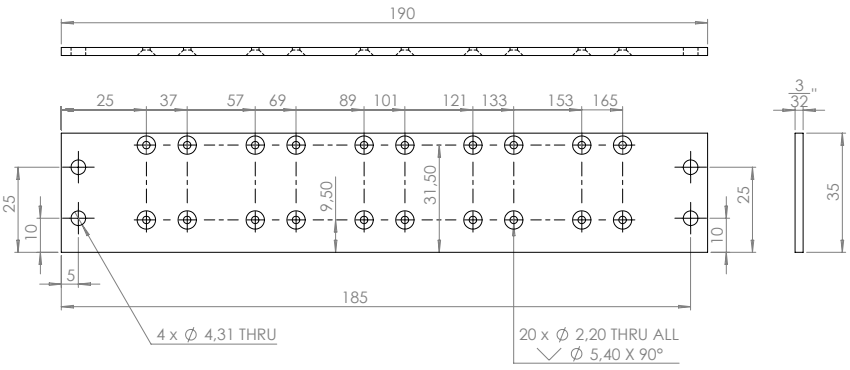

Camera plate
Scale 1:1, Rev A
Units in mm

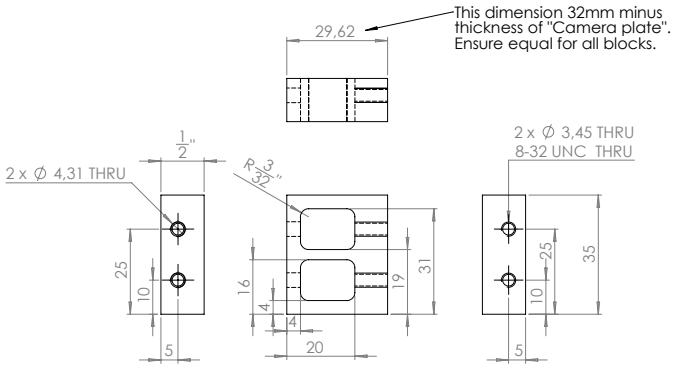

Spacer
Scale 1:1, Rev A
Units in mm

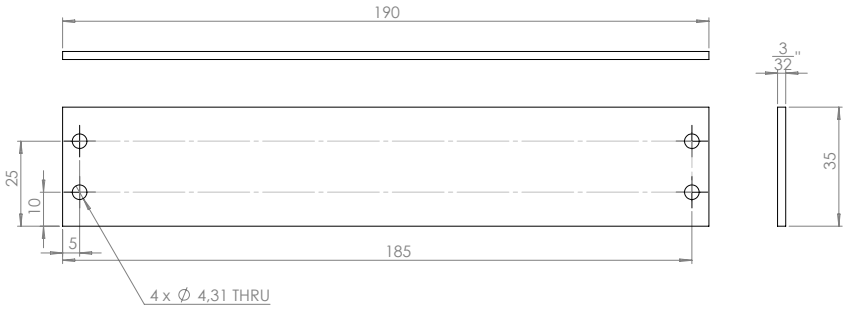

Top plate 1pcs
Scale 1:1, Rev A
Units in mm

B.2 MFG Holder

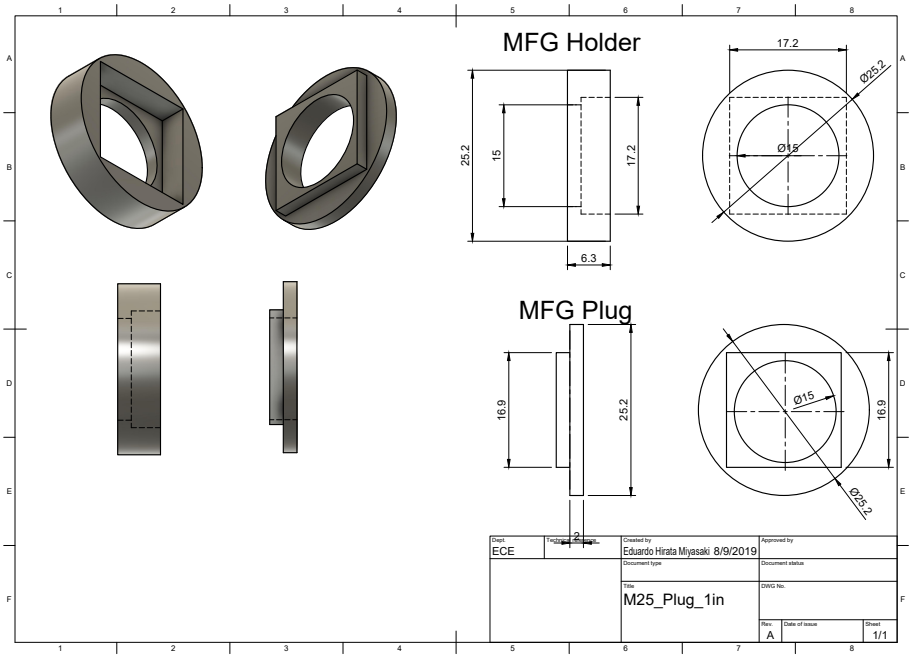
MFG Holder
17.2
Ø25.2
Ø15
25.2
15
17.2
6.3
MFG Plug
16.9
25.2
Ø15
16.9
Ø25.2
2
Dept.
ECE
Created by
Eduardo Hirata Miyasaki 8/9/2019
Approved by
Document type
Document status
Title
M25_Plug_1in
DWG No.
Rev.
A
Date of issue
Sheet
1/1

B.3 Home-built Microscope Objective and Stage Holder

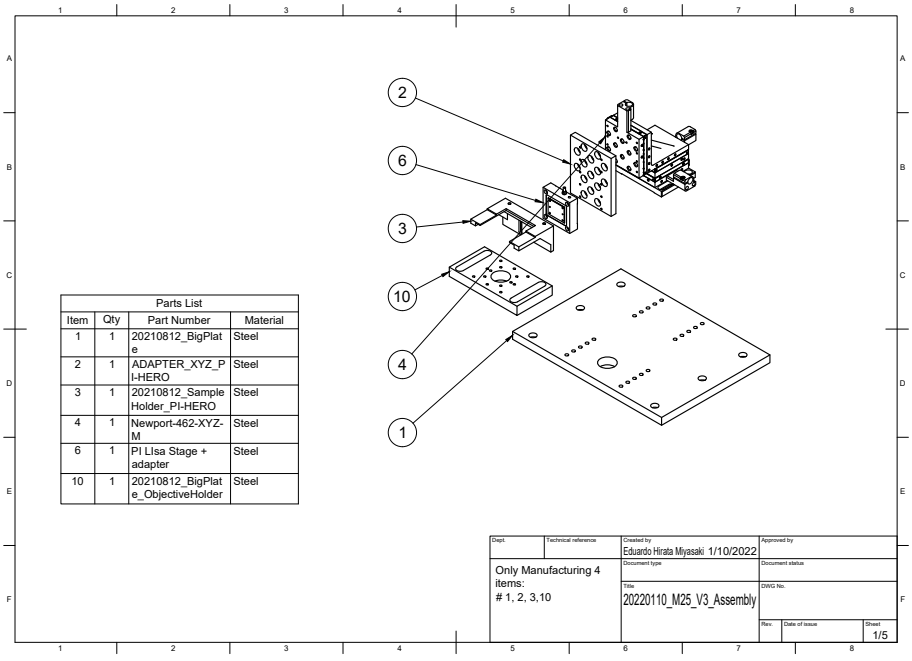

Parts List			
Item	Qty	Part Number	Material
1	1	20210812_BigPlate	Steel
2	1	ADAPTER_XYZ_PI-HERO	Steel
3	1	20210812_SampleHolder_PI-HERO	Steel
4	1	Newport-462-XYZ-M	Steel
6	1	PI LIsa Stage + adapter	Steel
10	1	20210812_BigPlate_ObjectiveHolder	Steel

Dept.	Technical reference	Created by: Eduardo Hirata Miyasaki 1/10/2022	Approved by
Only Manufacturing 4 items: # 1, 2, 3,10		Document type	Document status
		Title: 20220110_M25_V3_Assembly	DWG No.
		Rev.	Date of issue / Sheet: 1/5

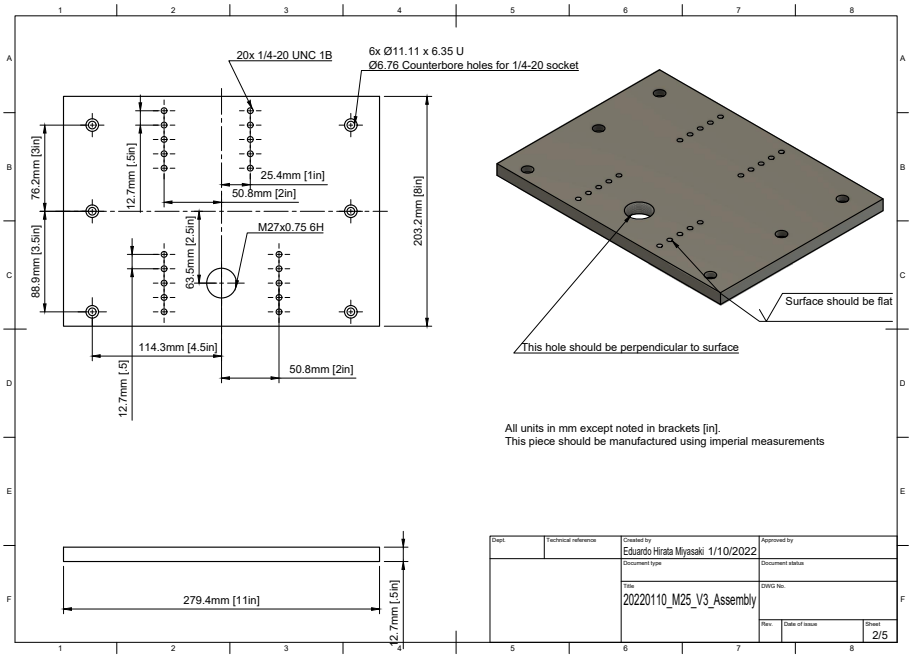
20x 1/4-20 UNC 1B
6x Ø11.11 x 6.35 U
Ø6.76 Counterbore holes for 1/4-20 socket
76.2mm [3in]
88.9mm [3.5in]
12.7mm [.5in]
25.4mm [1in]
50.8mm [2in]
M27x0.75 6H
63.5mm [2.5in]
203.2mm [8in]
114.3mm [4.5in]
50.8mm [2in]
12.7mm [.5]
Surface should be flat
This hole should be perpendicular to surface
All units in mm except noted in brackets [in].
This piece should be manufactured using imperial measurements
279.4mm [11in]
12.7mm [.5in]
Dept.
Technical reference
Created by
Eduardo Hirata Miyasaki 1/10/2022
Approved by
Document type
Document status
Title
20220110_M25_V3_Assembly
DWG No.
Rev.
Date of issue
Sheet
2/5

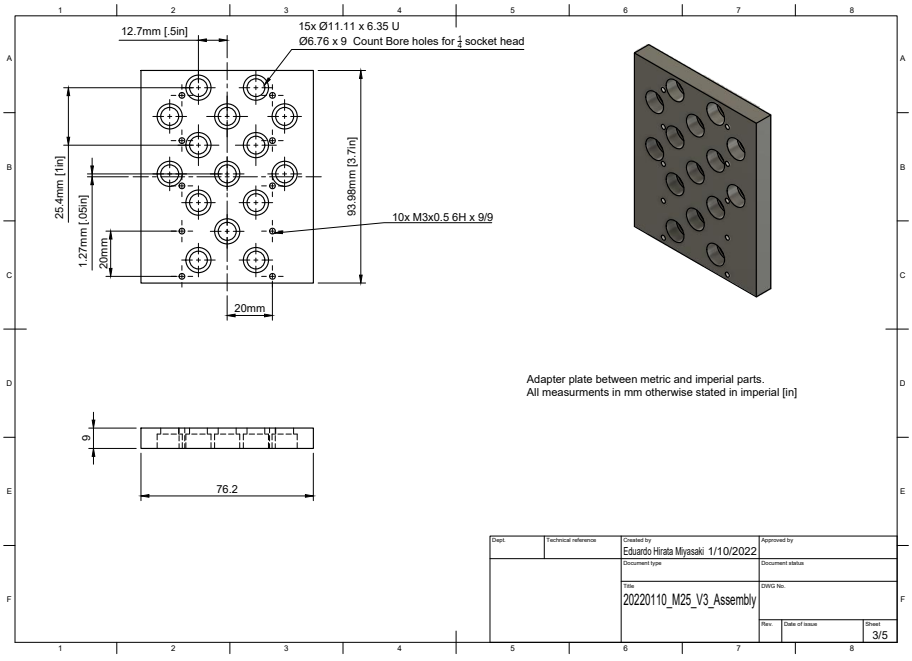
15x Ø11.11 x 6.35 U
Ø6.76 x 9 Count Bore holes for $\frac{1}{4}$ socket head
12.7mm [.5in]
25.4mm [1in]
1.27mm [.05in]
20mm
93.98mm [3.7in]
10x M3x0.5 6H x 9/9
20mm
9
76.2
Adapter plate between metric and imperial parts.
All measurments in mm otherwise stated in imperial [in]
Dept.
Technical reference
Created by
Eduardo Hirata Miyasaki 1/10/2022
Approved by
Document type
Document status
Title
20220110_M25_V3_Assembly
DWG No.
Rev.
Date of issue
Sheet
3/5

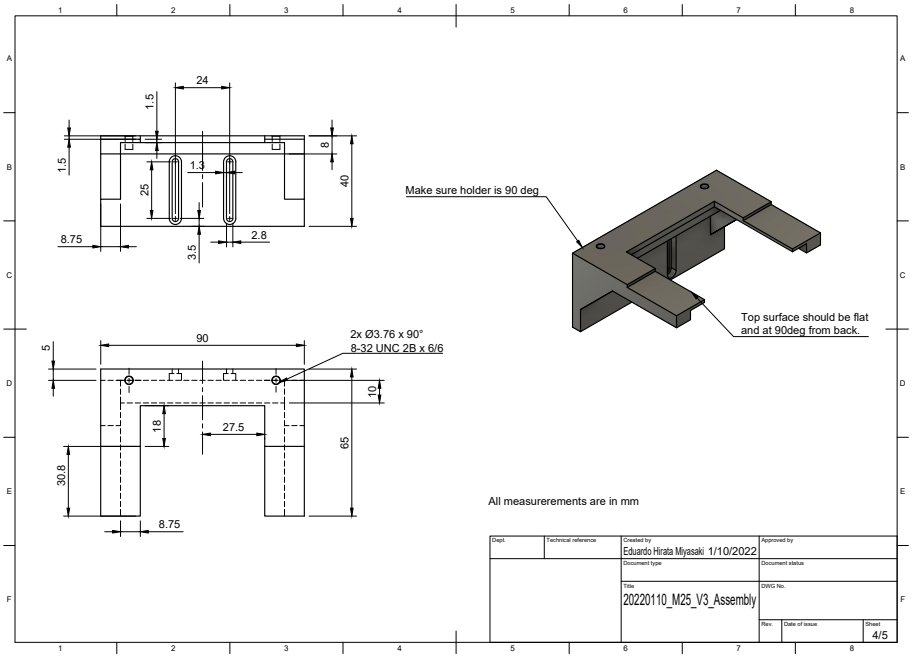
24
1.5
1.5
8
40
1.3
25
8.75
2.8
3.5
Make sure holder is 90 deg
Top surface should be flat
and at 90deg from back.
90
2x Ø3.76 x 90°
8-32 UNC 2B x 6/6
5
10
1.8
27.5
65
30.8
8.75
All measurerements are in mm
Dept.
Technical reference
Created by
Eduardo Hirata Miyasaki 1/10/2022
Approved by
Document type
Document status
Title
20220110_M25_V3_Assembly
DWG No.
Rev.
Date of issue
Sheet
4/5

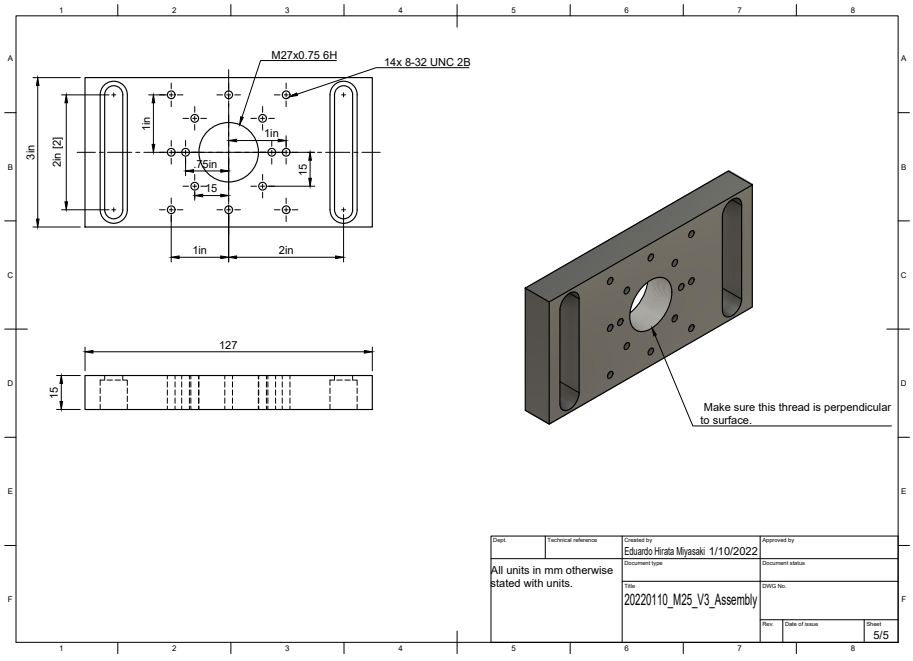
M27x0.75 6H
14x 8-32 UNC 2B
3in
2in [2]
1in
1in
.75in
15
15
1in
2in
127
15
Make sure this thread is perpendicular to surface.
All units in mm otherwise stated with units.
Eduardo Hirata Miyasaki 1/10/2022
20220110_M25_V3_Assembly
5/5

B.4 Lisa Stage Holder

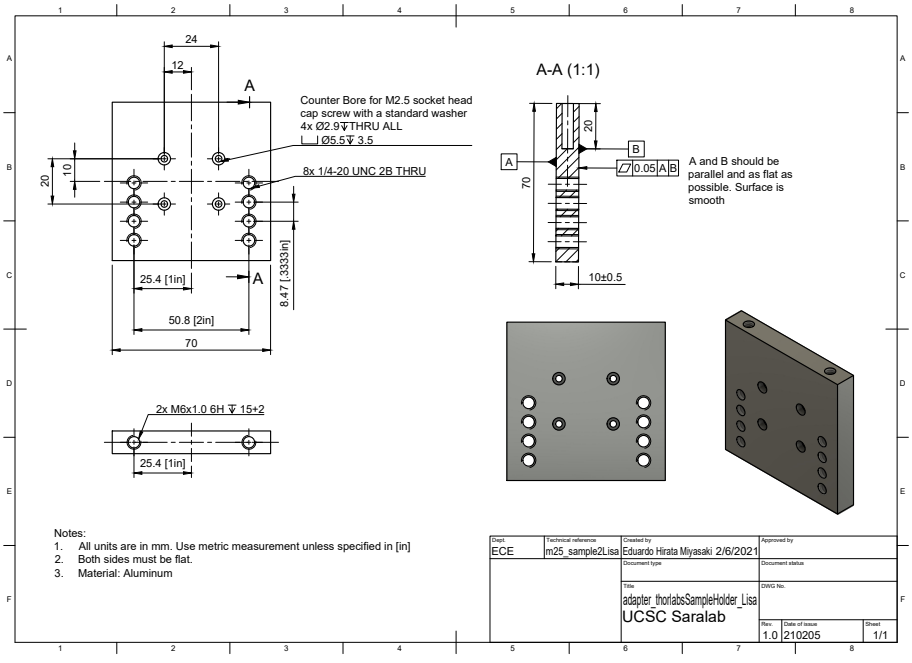

Notes:
1. All units are in mm. Use metric measurement unless specified in [in]
2. Both sides must be flat.
3. Material: Aluminum

Dept.	Technical reference	Created by	Approved by
ECE	m25_sample2Lisa	Eduardo Hirata Miyasaki 2/6/2021	
		Document type	Document status
		Title: adapter_thorlabsSampleHolder_Lisa UCSC Saralab	DWG No.
		Rev. 1.0	Date of issue 210205
			Sheet 1/1

Bibliography

[1] Sara Abrahamsson, Jiji Chen, Bassam Hajj, Sjoerd Stallinga, Alexander Y Katsov, Jan Wisniewski, Gaku Mizuguchi, Pierre Soule, Florian Mueller, Claire Dugast Darzacq, Xavier Darzacq, Carl Wu, Cornelia I Bargmann, David A Agard, Maxime Dahan, and Mats G L Gustafsson. Fast multicolor 3D imaging using aberration-corrected multifocus microscopy. *Nature Methods*, 10(1):60–63, January 2013.

[2] Sara Abrahamsson, Hans Blom, Ana Agostinho, Daniel C. Jans, Aurelie Jost, Marcel Müller, Linnea Nilsson, Kristoffer Bernhem, Talley J. Lambert, Rainer Heintzmann, and Hjalmar Brismar. Multifocus structured illumination microscopy for fast volumetric super-resolution imaging. *Biomedical Optics Express*, 8(9):4135, September 2017.

[3] Antoine Le Gall, Diego I. Cattoni, Baptiste Guilhas, Céline Mathieu-Demazière, Laura Oudjedi, Jean-Bernard Fiche, Jérôme Rech, Sara Abrahamsson, Heath Murray, Jean-Yves Bouet, and Marcelo Nollmann. Bacterial partition complexes segregate within the volume of the nucleoid. *Nature Communications*, 7:12107, July 2016.

[4] Max Born, Late Nobel Laureate Max Born, Emil Wolf, MAX AUTOR BORN, and A. B. Bhatia. *Principles of Optics: Electromagnetic Theory of Propagation, Interference and Diffraction of Light*. Cambridge University Press, October 1999. Google-Books-ID: nUHGpfNsGyUC.

[5] Joseph W. Goodman. *Introduction to Fourier optics*. McGraw-Hill series in electrical and computer engineering. McGraw-Hill, New York, 2nd ed edition, 1996.

[6] Osamu Shimomura, Frank H. Johnson, and Yo Saiga. Extraction, Purification and Properties of Aequorin, a Bioluminescent Protein from the Luminous Hydromedusan, Aequorea. *Journal of Cellular and Comparative Physiology*, 59(3):223–239, 1962. _eprint: https://onlinelibrary.wiley.com/doi/pdf/10.1002/jcp.1030590302.

[7] Jeff W. Lichtman and José-Angel Conchello. Fluorescence microscopy. *Nature Methods*, 2(12):910–919, December 2005.

[8] Christian A. Combs. Fluorescence Microscopy: A Concise Guide to Current Imaging Methods. *Current protocols in neuroscience / editorial board, Jacqueline N. Crawley ... [et al.]*, 0 2:Unit2.1, January 2010.

[9] Jan Huisken and Didier Y. R. Stainier. Selective plane illumination microscopy techniques in developmental biology. *Development (Cambridge, England)*, 136(12):1963–1975, June 2009.

[10] Wenze Li, Venkatakaushik Voleti, Evan Schaffer, Rebecca Vaadia, Wesley B. Grueber, Richard S. Mann, Elizabeth Hillman, Richard S. Mann, Elizabeth Hillman, Elizabeth Hillman, and Elizabeth Hillman. SCAPE Microscopy for High Speed, 3D Whole-Brain Imaging in Drosophila Melanogaster. In *Biomedical Optics 2016*, page BTu4D.3, Washington, D.C., April 2016. OSA.

[11] Abhishek Kumar, Yicong Wu, Ryan Christensen, Panagiotis Chandris, William Gandler, Evan McCreedy, Alexandra Bokinsky, Daniel A Colón-Ramos, Zhirong Bao, Matthew McAuliffe, Gary Rondeau, and Hari Shroff. Dual-view plane illumination microscopy for rapid and spatially isotropic imaging. *Nature protocols*, 9(11):2555–2573, November 2014.

[12] Manish Kumar, Sandeep Kishore, Jordan Nasenbeny, David L. McLean, and Yevgenia Kozorovitskiy. Integrated one- and two-photon scanned oblique plane illumination (SOPi) microscopy for rapid volumetric imaging. *Optics Express*, 26(10):13027, May 2018.

[13] C. Dunsby. Optically sectioned imaging by oblique plane microscopy. *Optics Express*, 16(25):20306–20316, December 2008. Publisher: Optica Publishing Group.

[14] Christine Grienberger and Arthur Konnerth. Imaging Calcium in Neurons. *Neuron*, 73(5):862–885, March 2012.

[15] Masoud Sepehri Rad, Yunsook Choi, Lawrence B. Cohen, Bradley J. Baker, Sheng Zhong, Douglas A. Storace, and Oliver R. Braubach. Voltage and Calcium Imaging of Brain Activity. *Biophysical Journal*, 113(10):2160–2167, November 2017.

[16] Michael Z. Lin and Mark J. Schnitzer. Genetically encoded indicators of neuronal activity. *Nature Neuroscience*, 19(9):1142–1153, September 2016. Number: 9 Publisher: Nature Publishing Group.

[17] Jerome Mertz. Strategies for volumetric imaging with a fluorescence microscope. *Optica*, 6(10):1261, October 2019.

[18] Florian O. Fahrbach, Fabian F. Voigt, Benjamin Schmid, Fritjof Helmchen, and Jan Huisken. Rapid 3D light-sheet microscopy with a tunable lens. *Optics Express*, 21(18):21010, September 2013.

[19] Edward J. Botcherby, Rimas Juskaitis, Martin J. Booth, and Tony Wilson. Aberration-free optical refocusing in high numerical aperture microscopy. *Optics Letters*, 32(14):2007, July 2007.

[20] Marc Levoy, Ren Ng, Andrew Adams, Matthew Footer, and Mark Horowitz. Light field microscopy. In *ACM SIGGRAPH 2006 Papers*, SIGGRAPH '06, pages 924–934, New York, NY, USA, July 2006. Association for Computing Machinery.

[21] Fanglin Linda Liu, Grace Kuo, Nick Antipa, Kyrollos Yanny, Laura Waller, and Laura Waller. Fourier DiffuserScope: single-shot 3D Fourier light field microscopy with a diffuser. *Optics Express*, 28(20):28969–28986, September 2020. Publisher: Optica Publishing Group.

[22] Nils Wagner, Nils Norlin, Jakob Gierten, Gustavo de Medeiros, Bálint Balázs, Joachim Wittbrodt, Lars Hufnagel, and Robert Prevedel. Instantaneous isotropic volumetric imaging of fast biological processes. *Nature Methods*, 16(6):497–500, June 2019.

[23] Manuel Martínez-Corral and Bahram Javidi. Fundamentals of 3D imaging and displays: a tutorial on integral imaging, light-field, and plenoptic systems. *Advances in Optics and Photonics*, 10(3):512, September 2018.

[24] Sheng Xiao, Howard Gritton, Hua-An Tseng, Dana Zemel, Xue Han, and Jerome Mertz. High-contrast multifocus microscopy with a single camera and z-splitter prism. *Optica*, 7(11):1477, November 2020.

[25] Prashant Prabhat, Sripad Ram, E. Sally Ward, and Raimund J. Ober. Simultaneous imaging of different focal planes in fluorescence microscopy for the study of cellular dynamics in three dimensions. *IEEE transactions on nanobioscience*, 3(4):237–242, December 2004.

[26] Paul M. Blanchard and Alan H. Greenaway. Simultaneous multiplane imaging with a distorted diffraction grating. *Applied Optics*, 38(32):6692, November 1999.

[27] Christine Grienberger and Arthur Konnerth. Imaging calcium in neurons. *Neuron*, 73(5):862–885, March 2012.

[28] M. J. Berridge, P. Lipp, and M. D. Bootman. The versatility and universality of calcium signalling. *Nature Reviews. Molecular Cell Biology*, 1(1):11–21, October 2000.

[29] F. Helmchen, J. G. Borst, and B. Sakmann. Calcium dynamics associated with a single action potential in a CNS presynaptic terminal. *Biophysical Journal*, 72(3):1458–1471, March 1997.

[30] Tsai-Wen Chen, Trevor J. Wardill, Yi Sun, Stefan R. Pulver, Sabine L. Renninger, Amy Baohan, Eric R. Schreiter, Rex A. Kerr, Michael B. Orger, Vivek Jayaraman, Loren L. Looger, Karel Svoboda, and Douglas S. Kim. Ultra-sensitive fluorescent proteins for imaging neuronal activity. *Nature*, 499(7458):295–300, July 2013.

[31] Gloster Aaron and Rafael Yuste. Reverse optical probing (ROPING) of neocortical circuits. *Synapse (New York, N.Y.)*, 60(6):437–440, November 2006.

[32] Jan Huisken, Jim Swoger, Filippo Del Bene, Joachim Wittbrodt, and Ernst H. K. Stelzer. Optical sectioning deep inside live embryos by selective plane illumination microscopy. *Science (New York, N.Y.)*, 305(5686):1007–1009, August 2004.

[33] Yuji Takahara, Norio Matsuki, and Yuji Ikegaya. Nipkow confocal imaging from deep brain tissues. *Journal of Integrative Neuroscience*, 10(1):121–129, March 2011.

[34] W. Denk, J. H. Strickler, and W. W. Webb. Two-photon laser scanning fluorescence microscopy. *Science (New York, N.Y.)*, 248(4951):73–76, April 1990.

[35] Yongmin Cho, Charles L. Zhao, and Hang Lu. Trends in high-throughput and functional neuroimaging in Caenorhabditis elegans. *Wiley Interdisciplinary Reviews: Systems Biology and Medicine*, 9(3), May 2017. Publisher: Wiley-Blackwell.

[36] Daniel B. Allan, Thomas Caswell, Nathan C. Keim, Casper M. van der Wel, and Ruben W. Verweij. soft-matter/trackpy: Trackpy v0.5.0, April 2021.

[37] Jean-Yves Tinevez, Nick Perry, Johannes Schindelin, Genevieve M. Hoopes, Gregory D. Reynolds, Emmanuel Laplantine, Sebastian Y. Bednarek, Spencer L. Shorte, and Kevin W. Eliceiri. TrackMate: An open and extensible platform for single-particle tracking. *Methods*, 115:80–90, February 2017.

[38] Marco A. Catipovic, Paul M. Tyler, Josef G. Trapani, and Ashley R. Carter. Improving the quantification of Brownian motion. *American Journal of Physics*, 81(7):485–491, July 2013. Publisher: American Association of Physics Teachers.

[39] J Gray and H W Lissmann. THE LOCOMOTION OF NEMATODES. *F.exp.bio*, (41):24, 1964.

[40] Julijana Gjorgjieva, David Biron, and Gal Haspel. Neurobiology of Caenorhabditis elegans Locomotion: Where Do We Stand? *BioScience*, 64(6):476–486, June 2014.

[41] Juan Nunez-Iglesias, Adam J. Blanch, Oliver Looker, Matthew W. Dixon, and Leann Tilley. A new Python library to analyse skeleton images confirms malaria parasite remodelling of the red blood cell membrane skeleton. *PeerJ*, 6:e4312, February 2018.

[42] Nicholas Sofroniew, Talley Lambert, Kira Evans, Juan Nunez-Iglesias, Grzegorz Bokota, Philip Winston, Gonzalo Peña-Castellanos, Kevin Yamauchi, Matthias Bussonnier, Draga Doncila Pop, Ahmet Can Solak, Ziyang Liu, Pam Wadhwa, Alister Burt, Genevieve Buckley, Andrew Sweet, Lukasz Migas, Volker Hilsenstein, Lorenzo Gaifas, Jordão Bragantini, Jaime Rodríguez-Guerra, Hector Muñoz, Jeremy Freeman, Peter Boone, Alan Lowe, Christoph Gohlke, Loic Royer, Andrea PIERRÉ, Hagai Har-Gil, and Abigail McGovern. napari: a multi-dimensional image viewer for Python, May 2022.

[43] Stefano Berri, Jordan H. Boyle, Manlio Tassieri, Ian A. Hope, and Netta Cohen. Forward locomotion of the nematode C. elegans is achieved through modulation of a single gait. *HFSP journal*, 3(3):186–193, June 2009.

[44] Lan Deng, Jack E. Denham, Charu Arya, Omer Yuval, Netta Cohen, and Gal Haspel. Inhibition Underlies Fast Undulatory Locomotion in Caenorhabditis elegans. *eNeuro*, 8(2):ENEURO.0241–20.2020, March 2021.

[45] Gal Haspel, Kristen E. Severi, Lisa J. Fauci, Netta Cohen, Eric D. Tytell, and Jennifer R. Morgan. Resilience of neural networks for locomotion. *The Journal of Physiology*, 599(16):3825–3840, August 2021.

[46] Arthur Edelstein, Nenad Amodaj, Karl Hoover, Ron Vale, and Nico Stuurman. Computer Control of Microscopes Using µManager. *Current Protocols in Molecular Biology*, 92(1):14.20.1–14.20.17, 2010. _eprint: https://onlinelibrary.wiley.com/doi/pdf/10.1002/0471142727.mb1420s92.

[47] Sara Abrahamsson, Molly McQuilken, Shalin B. Mehta, Amitabh Verma, Johannes Larsch, Rob Ilic, Rainer Heintzmann, Cornelia I. Bargmann, Amy S. Gladfelter, and Rudolf Oldenbourg. MultiFocus Polarization Microscope (MF-PolScope) for 3D polarization imaging of up to 25 focal planes simultaneously. *Optics Express*, 23(6):7734, March 2015.